

Kinematic splitting algorithm for fluid-structure interaction in hemodynamics

M. Lukáčová - Medviďová^{1*}, G. Rusnáková^{1,2} and A. Hundertmark-Zaušková¹

Abstract

In this paper we study a kinematic splitting algorithm for fluid-structure interaction problems. This algorithm belongs to the class of loosely-coupled fluid-structure interaction schemes. We will present stability analysis for a coupled problem of non-Newtonian shear-dependent fluids in moving domains with viscoelastic boundaries. Fluid flow is described by the conservation laws with nonlinearities in convective and diffusive terms. For simplicity of presentation the structure is modelled by the generalized string equation, but the results presented in the paper may be generalized to more complex structure models. The arbitrary Lagrangian-Eulerian approach is used in order to take into account moving computational domain. Numerical experiments including numerical error analysis and comparison of hemodynamic parameters for Newtonian and non-Newtonian fluids demonstrate reliability of the proposed scheme.

Key words: fluid-structure interaction, non-Newtonian fluids, stability, hemodynamic wall parameters, stenosis, bifurcation

1 INTRODUCTION

The study of blood flow in human cardiovascular system is of great interest. Diseases of cardiovascular system such as atherosclerosis, i.e. hardening of arteries, are the main cause of illnesses and death in Western countries. Atherosclerotic plaque narrows the arteries and may block the transfer of oxygen-rich blood from the heart to other parts of body [29]. In general, there are two types of plaques. Hard plaque is stable and causes the artery walls hardening and thickening. On the other side the soft plaque is very unstable and tends to break vessel walls and enter the bloodstream. The resulting blood clots can partially restrict or totally block blood flow [1]. In this article we focus on modelling blood flow in arteries with stenosis caused by a stable plaque formation. Up to now the complex process of atherogenesis is not completely understood [12]. The questions of how the arteries become damaged, how plaque develops and changes over time are still an active area of medical research [29]. In the recent decades a big progress has been done in clinical research as well as in mathematical modelling of cardiovascular system. Geometric reconstruction techniques and medical imaging give us information about geometries of different types of blood vessels that is crucial in order to bring mathematical modelling closer to real applications [5, 6, 9, 10, 13, 23, 33, 50, 51, 52, 53]. Furthermore, results from numerical experiments, that are confirmed by in vivo experiments, encourage the use of sophisticated numerical methods to simulate blood flow in mostly abnormal blood vessels and give information about regions with increased plaque danger or thrombosis occurrence [1, 44, 47, 49].

Importance of the non-Newtonian blood rheology is a frequently discussed topic. Considering blood flow in large arteries of healthy people blood is typically modelled as a Newtonian fluid [25]. Thus the Cauchy stress tensor depends linearly on the rate of the deformation tensor. However, in vessels with

¹Department of Mathematics, Johannes Gutenberg University, Staudingerweg 9, 550 99 Mainz, Germany

²Institute of Mathematics, Pavol Jozef Šafárik University, Jesenná 5, 040 01 Košice, Slovakia

* Corresponding author: lukacova@uni-mainz.de, Tel.: +49-6131-39-22831; Fax: +49-6131-39-23331

smaller diameter or dealing with patients with a cardiovascular disease, the so-called non-Newtonian models for blood viscosity should be considered [7, 25, 32, 55, 56]. Soulis et al. [48] studied the non-Newtonian behaviour with respect to a cardiac cycle. They found the non-Newtonian rheology to be relevant for approximately 30% of one cardiac cycle. However, both models, the Newtonian as well as the non-Newtonian, predicted crucial areas with low wall shear stress at the same positions. Ardakani et al. [2] focused on viscosity blood models in modelling of blood flow in stenosed carotid bifurcations. They showed that the non-Newtonian effect is more visible dealing with ideal model geometries than with geometries obtained from real patients. Moreover, considering real geometries, difference between the Newtonian and the non-Newtonian constitutive blood model depends on the position in the vessel. Especially in a carotid bifurcation, differences are more visible in the sinus bulb area than in other parts of artery.

Studying blood flow of patients with a cardiovascular disease, the choice of appropriate hemodynamic factors plays an important role. A significant index is the so-called shear rate. High shear rate in arteries plays a key role for the development of thrombosis. Also considering blood flow through a stenosed region, high shear areas appear, even if only for a short time. In these cases a plaque rupture can occur already after 7ms of high shear flow [29]. An important hemodynamic indicator of atherosclerosis is the so-called wall shear stress. It is well-known that high wall shear stress tends to a mechanical damage of inner parts of vessel walls. Moreover, even too low wall shear stress is not desirable since it can promote the accumulation of plaque. In addition, a mechanical sign of atherosclerotic diseases is formation of vortex structures and even turbulence. The latter increases the kinetic energy and also creates a stagnant blood flow. Stagnation regions occur usually in the areas with sharp curvatures such as those present at vessel bifurcation branchings or in severe stenosed vessels. Blood coagulation in these complex geometries can lead to formation of blood clots and induce ischemia, heart attack or an other pathological situations. In addition, devices implanted in the cardiovascular system, such as stents or prosthetic heart valves, can interrupt normal biochemical conditions too. Recently, there is an active mathematical research focused on blood coagulation, the modelling of equilibrium and of its stability, see, e.g., [1, 47] and the references therein.

In the recent years there has been an increasing interest in the development of efficient numerical algorithms for fluid-structure interaction in hemodynamics, see, e.g., [11, 13, 14, 18, 21, 27, 32, 39, 40, 43, 53] just to mention some of them. In general, there are two ways to construct a numerical scheme for coupled fluid-structure interaction problems. Monolithic algorithms solve the whole fully coupled problem at once. This requires a new coupled solver and the algorithms are thus less modular. They belong to the class of strongly coupled schemes. An alternative, quite popular, approach represents the partitioned algorithms that allow the use of different solvers for different physical subproblems. Among the partitioned algorithms we may distinguish between strongly and weakly coupled methods. If the weak coupling is used a possible imbalance of coupling conditions and corresponding artificial added mass effects may cause instability in particular for problems arising in hemodynamics. One way to overcome the stability issue is to realize sub-iterations per each time step (implicit or strong coupling) that balance out the coupling conditions, see, e.g., [18, 30, 37, 53]. Recently, some new loosely coupled algorithms (explicit coupling) have been proposed in [3, 11, 14, 16, 18, 27, 40].

The main goal of the present paper is to analyse theoretically as well as experimentally a new loosely coupled kinematic splitting algorithm. In our work we were inspired by the recent paper of Guidoboni et al. [27], where a novel way to avoid instabilities and the necessity of introducing additional stabilization terms in fluid-structure interaction algorithms has been presented, see also the recent paper of Muha and Čanić where the analogous operator splitting algorithm has been used to show the existence of weak solution to the FSI problem. Our approach is more general than [27] because we allow the use of the second order splitting method and the non-Newtonian fluid rheology. Moreover we analyse theoretically the fully nonlinear coupling between the non-Newtonian fluid and linear structure, taking the mesh movement into account. Here we also point out the role of the geometric conservation law in order to get an unconditionally stable coupling. Note that in [27] the stability analysis was performed only for the linear Stokes equations and the fluid domain was kept fixed. For simplicity of presentation we will restrict ourselves to a simple structural model, the generalized string model, allowing however a non-constant vessel radius in order to model, e.g., stenotic occlusions. Theoretical results presented here can

be generalized to more complex linear structures, such as those used, e.g., in [13, 18, 40]. On the other hand, our aim is to emphasize the non-Newtonian blood rheology and to consider the shear-thinning behaviour of blood. The coupled fluid-structure interaction model considered in the present paper is simple enough to present a detailed numerical analysis, but it inherits the most important difficulties important to understand complex physiological behaviour of three-dimensional vascular flow.

The plan of the present paper is following. In Section 2 we will describe the mathematical model of blood flow in compliant vessels. We use the conservation laws for incompressible fluids together with an elastic model of vessel walls. Section 3 is devoted to the numerical analysis of the loosely-coupled fluid-structure interaction algorithm based on the kinematic splitting. We will derive an energy estimate for discrete coupled fluid-structure interaction problem that includes nonlinearities in both the convective and the diffusive terms as well as in the geometric coupling.

Finally, in Section 4 we will present results of numerical experiments. Since we are interested in modelling of blood flow in stenosed regions, we will consider preferably non-Newtonian constitutive models. They will be compared with the results obtained for the Newtonian fluid. A comparison will be done for different types of geometry such as a single artery with a stenotic occlusion as well as a carotid arterial bifurcation. Numerical experiments will be realized for simplified two-dimensional domains representing cuts of compliant vessels. An example of possible generalization for more realistic three-dimensional flows is presented in Section 4.6.

The numerical error analysis will be performed for a simplified geometry and compared with the so-called global iterative approach [30]. Moreover, a comparison in terms of the hemodynamic wall parameters such as the wall-shear stress and the oscillatory shear index will be presented. The experimental analysis of convergence in both space and time confirms stability and good resolution of the proposed scheme.

2 MATHEMATICAL MODEL

In what follows we describe the mathematical model of blood flow in a compliant vessel. Motion of incompressible fluid flow is governed by the momentum and the continuity equation

$$\rho_f \left[\frac{\partial \mathbf{u}}{\partial t} + (\mathbf{u} \cdot \nabla) \mathbf{u} \right] - \nabla \cdot \left[2\mu(|\mathbf{D}(\mathbf{u})|) \mathbf{D}(\mathbf{u}) \right] + \nabla p = \mathbf{f}, \quad \nabla \cdot \mathbf{u} = 0 \quad \text{in } \Omega_t, \quad (1)$$

where Ω_t is a time-dependent computational domain and $t \in I = [0, T]$. The unknowns are the fluid velocity $\mathbf{u} = \mathbf{u}(\mathbf{x}, t) = (u_1, u_2)^T$ and pressure $p = p(\mathbf{x}, t)$. Moreover, $\mathbf{D} = 1/2(\nabla \mathbf{u} + \nabla \mathbf{u}^T)$ denotes the rate of the deformation tensor, \mathbf{f} describes a possible forcing term, ρ_f denotes the fluid density that is assumed to be a constant and $\mu(|\mathbf{D}(\mathbf{u})|)$ is the viscosity function describing the non-Newtonian behaviour of blood [25]. In the literature we can find several models to describe non-Newtonian behaviour of blood. In this work we will use the **Carreau model**

$$\mu(|\mathbf{D}(\mathbf{u})|) = \mu_\infty + (\mu_0 - \mu_\infty) \left[1 + 2(\lambda|\mathbf{D}(\mathbf{u})|)^2 \right]^{\frac{q-2}{2}} \quad (2)$$

and the **Yeleswarapu viscosity model**

$$\mu(|\mathbf{D}(\mathbf{u})|) = \mu_\infty + (\mu_0 - \mu_\infty) \left[\frac{1 + \ln(1 + \sqrt{2}\Lambda|\mathbf{D}(\mathbf{u})|)}{1 + \sqrt{2}\Lambda|\mathbf{D}(\mathbf{u})|} \right]. \quad (3)$$

Here μ_∞ and μ_0 are the asymptotic values of viscosity, i.e.

$$\mu_\infty := \lim_{|\mathbf{D}(\mathbf{u})| \rightarrow \infty} \mu(|\mathbf{D}(\mathbf{u})|), \quad \mu_0 := \lim_{|\mathbf{D}(\mathbf{u})| \rightarrow 0} \mu(|\mathbf{D}(\mathbf{u})|).$$

The parameters λ , Λ and q are given constants [55], see also Tab. 2 for typical physiological values used for blood and Fig. 1 for the corresponding graphs. We note also that the dependence of viscosity on the rate of the deformation tensor is sometimes expressed in terms of the so-called shear rate, that is in the

two-dimensional case defined by $\dot{\gamma} := \sqrt{2 \operatorname{tr}(\mathbf{D}^2)}$, cf. [7, 8, 25, 55]. From the definition (2) we see that for $q > 2$ viscosity increases with increasing shear rate ($\mu_0 < \mu_\infty$), while for $q < 2$ viscosity decreases with increasing shear rate ($\mu_0 > \mu_\infty$). The first situation describes the so-called shear-thickening fluids and the second situation represents the so-called shear-thinning fluids. If $q = 2$, then we obtain the simplest behaviour corresponding to Newtonian fluids. The Yeleswarapu model describes only the shear-thinning behaviour.

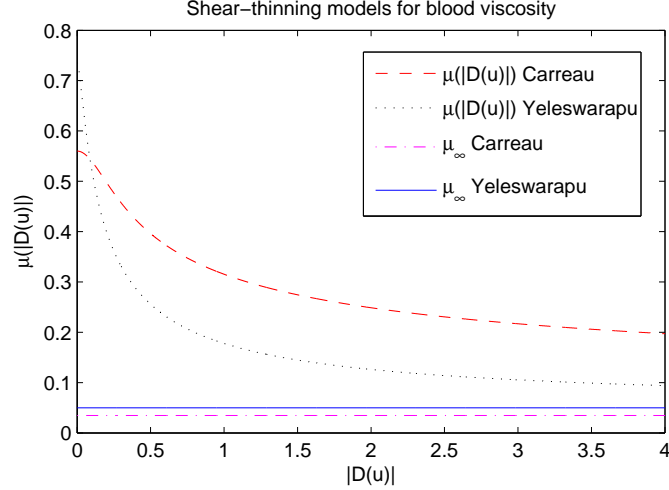


Figure 1: Viscosity function for non-Newtonian models (2) and (3) and asymptotic viscosities μ_∞ for (2) and (3) fit for the physiological data from Tab. 2.

In order to capture the movement of a deformable computational domain and preserve the rigidness of inflow and outflow parts, the conservation laws are rewritten using the so-called ALE (**A**rbitrary **L**agrangian-**E**ulerian) mapping \mathcal{A}_t , see Fig. 25. Assuming Ω_{ref} to be bounded with $\partial\Omega_{ref}$ Lipschitz continuous, we have $\Omega_t := \mathcal{A}_t(\Omega_{ref})$ is bounded and $\partial\Omega_t$ is Lipschitz continuous. Throughout the paper we will assume that the ALE mapping \mathcal{A}_t is enough smooth. In particular we assume that $\mathcal{A}_t \in W^{1,\infty}(\Omega_{ref})$, $\mathcal{A}_t^{-1} \in W^{1,\infty}(\Omega_t)$, $\forall t \in I$, where Ω_{ref} is a two-dimensional bounded reference domain with the Lipschitz continuous boundary. Indeed, one can construct analogously as in [39] the ALE mapping obeying the above regularity and show that $v \circ \mathcal{A}_t$ is an isomorphism from $L^q(0, T; W^{1,q}(\Omega_{ref}))$ onto $L^q(0, T; W^{1,q}(\Omega_t))$ and from $L^\infty(0, T; L^2(\Omega_{ref}))$ onto $L^\infty(0, T; L^2(\Omega_t))$. We will present one such example in Section 3.1.

Introducing the so-called ALE derivative

$$\frac{\mathcal{D}^A \mathbf{u}(\mathbf{x}, t)}{\mathcal{D}t} := \left. \frac{\partial \mathbf{u}(\mathbf{Y}, t)}{\partial t} \right|_{\mathbf{Y}=\mathcal{A}_t^{-1}(\mathbf{x})} = \left. \frac{\partial \mathbf{u}(\mathbf{x}, t)}{\partial t} \right|_{\mathbf{x}} + \mathbf{w}(\mathbf{x}, t) \cdot \nabla \mathbf{u}(\mathbf{x}, t) \quad \text{for } \mathbf{x} \in \Omega_t, \mathbf{Y} \in \Omega_{ref} \quad (4)$$

we can define the domain velocity

$$\mathbf{w}(\mathbf{x}, t) := \left. \frac{\partial \mathcal{A}_t(\mathbf{Y})}{\partial t} \right|_{\mathbf{Y}=\mathcal{A}_t^{-1}(\mathbf{x})} = \frac{\partial \mathbf{x}}{\partial t} \quad \text{for } \mathbf{x} \in \Omega_t, \mathbf{Y} \in \Omega_{ref}$$

and rewrite the governing equations (1) into the form that takes into account specific time-dependent behaviour of the domain, i.e.

$$\rho_f \left[\frac{\mathcal{D}^A \mathbf{u}}{\mathcal{D}t} + ((\mathbf{u} - \mathbf{w}) \cdot \nabla) \mathbf{u} \right] - \nabla \cdot \left[2\mu(|\mathbf{D}(\mathbf{u})|) \mathbf{D}(\mathbf{u}) \right] + \nabla p = \mathbf{f}, \quad \nabla \cdot \mathbf{u} = 0 \quad \text{in } \Omega_t, t \in I. \quad (5)$$

For realistic hemodynamic simulations fully three-dimensional vascular flow should be considered. However, the main aim of this paper is to analyse theoretically as well as experimentally a loosely coupled kinematic splitting technique and apply it to fully nonlinear coupling between the non-Newtonian shear-dependent fluid and a linear structure. Thus, for simplicity of presentation and in order to point out

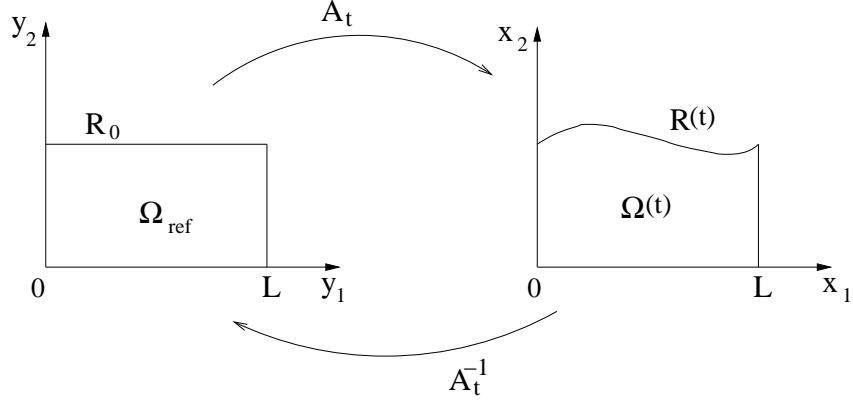


Figure 2: ALE mapping \mathcal{A}_t with a moving boundary and a symmetry axis.

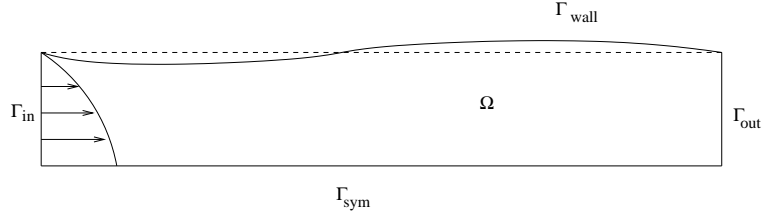


Figure 3: Computational domain geometry.

clearly the conceptual difficulties appearing in hemodynamic flows we will consider a simplified structural model, the so-called generalized string model, that has been derived for axially symmetric configurations [30, 53] and used for several real applications [43]; in Section 4.6 an example of generalization to more realistic three-dimensional flows will be presented.

We consider a two-dimensional fluid domain

$$\Omega_t := \{(x_1, x_2) \in \mathbb{R}^2, t \in I : 0 < x_1 < L, 0 < x_2 < R_0(x_1) + \eta(x_1, t) =: R(x_1, t)\}$$

with a given reference radius $R_0(x_1)$ and unknown wall displacement function $\eta(x_1, t)$. We assume that the upper boundary Γ_{wall} is deformable and the lower one Γ_{sym} is the axis of symmetry, cf. Fig. 3.

Further, assuming that $\partial_{x_1}\eta(x_1, t) \ll 1$ and using the theory of linear elasticity the following form of the generalized string model describing the wall displacement $\eta = \eta(x_1, t)$ in the radial direction can be derived [30, 53]

$$\frac{\partial^2 \eta}{\partial t^2} - a \frac{\partial^2 (\eta + R_0)}{\partial x_1^2} + b\eta - c \frac{\partial^3 \eta}{\partial t \partial x_1^2} = H(\mathbf{u}, p) \quad \text{on } \Gamma_{wall}^0, \quad (6)$$

where

$$\Gamma_{wall}^0 := \{(x_1, x_2) \in \mathbb{R}^2 : 0 < x_1 < L, x_2 = R_0(x_1)\} \quad (7)$$

and $H(\mathbf{u}, p)$ represents the forces exhibited by the normal fluid stress acting on the elastic vessel wall and transformed to Γ_{wall}^0

$$H(\mathbf{u}, p) := - \frac{\left((\mathbf{T} + P_{ext} \mathbf{I}) \mathbf{n} \right) \Big|_{\Gamma_{wall}^0} \cdot \mathbf{e}_r}{\rho_s h} \frac{R}{R_0} \frac{\sqrt{1 + (\partial_{x_1} R)^2}}{\sqrt{1 + (\partial_{x_1} R_0)^2}}, \quad R = R_0 + \eta. \quad (8)$$

The term with square roots corresponds to the Jacobian of the transformation between the Eulerian framework used for the description of fluid and the Lagrangian framework used for the structure. Further, \mathbf{T} denotes the Cauchy stress tensor defined by

$$\mathbf{T} = -p\mathbf{I} + 2\mu(|\mathbf{D}(\mathbf{u})|) \mathbf{D}(\mathbf{u}),$$

the unit normal vector \mathbf{n} on Γ_{wall} and the unit vector in the radial direction \mathbf{e}_r are defined by

$$\mathbf{n} = \frac{1}{\sqrt{1 + (\partial_{x_1} R)^2}} \begin{pmatrix} -\frac{\partial R}{\partial x_1} \\ 1 \end{pmatrix}^T, \quad \mathbf{e}_r = (0, 1)^T,$$

respectively, and P_{ext} denotes the external pressure arising from surrounding tissues. Here and in what follows we will use a shorter notation $f_{x_1} := \partial f / \partial x_1$ and $f_{x_1 x_1} := \partial^2 f / \partial x_1^2$. Further parameters in (6) are defined as

$$a = \frac{|\sigma_{x_1}|}{\rho_s} \left[1 + \left(\frac{\partial R_0}{\partial x_1} \right)^2 \right]^{-2}, \quad b = \frac{E}{\rho_s (1 - \tilde{\xi}^2) R_0^2}, \quad c = \frac{\gamma}{\rho_s h}. \quad (9)$$

Here ρ_s is the wall density, h is the wall thickness, E denotes the Young modulus of elasticity, $|\sigma_{x_1}| = G\kappa$ is the longitudinal stress, $G = E/(2(1 + \tilde{\xi}))$ denotes the shear modulus, $\tilde{\xi}$ is the Poisson ratio, κ is the Timoshenko shear correction factor and γ is a viscoelasticity constant.

The coupled fluid-structure interaction problem (5) and (6) is equipped with the following initial conditions

$$\mathbf{u} = \mathbf{u}_0 \quad \text{in } \Omega_0, \quad (10)$$

$$\eta = 0, \quad \frac{\partial \eta}{\partial t} = \mathbf{u}_0|_{\Gamma_{wall}^0} \cdot \mathbf{e}_r \quad \text{on } \Gamma_{wall}^0. \quad (11)$$

Boundary conditions read as follows

$$\left(\mathbf{T}(\mathbf{u}, p) - \frac{\rho_f}{2} |\mathbf{u}|^2 \mathbf{I} \right) \cdot \mathbf{n} = -(P_{in} \mathbf{I}) \cdot \mathbf{n}, \quad \text{on } \Gamma_{in}, t \in I, \quad (12)$$

$$\left(\mathbf{T}(\mathbf{u}, p) - \frac{\rho_f}{2} |\mathbf{u}|^2 \mathbf{I} \right) \cdot \mathbf{n} = -(P_{out} \mathbf{I}) \cdot \mathbf{n}, \quad \text{on } \Gamma_{out}, t \in I, \quad (13)$$

$$\frac{\partial u_1}{\partial x_2} = 0, \quad u_2 = 0, \quad \text{on } \Gamma_{sym}, t \in I, \quad (14)$$

$$\eta(0, t) = \eta_1, \quad \eta(L, t) = \eta_2, \quad \text{for } t \in I. \quad (15)$$

Here P_{in}, P_{out} represent the inflow/outflow pressure that can be obtained by measurements. Conditions (12) and (13) are called the kinematic pressure conditions. They are a variant of the well-known ‘‘do nothing’’ boundary conditions in the case that the Bernoulli pressure $p + \rho_f |\mathbf{u}|^2 / 2$ is taken into account, cf. [25, 28, 30]. We would like to point out that using the boundary conditions (12) and (13) the existence of weak solution to the coupled fluid-structure interaction model can be shown, see [20, 31]. The fluid and the structure are coupled through the following condition

$$\mathbf{u} = \mathbf{w} := \left(0, \frac{\partial \eta}{\partial t} \right)^T \quad \text{on } \Gamma_{wall}(t), \quad (16)$$

where

$$\Gamma_{wall}(t) := \{(x_1, x_2) \in \mathbb{R}^2, t \in I : 0 < x_1 < L, x_2 = R_0(x_1) + \eta(x_1, t)\}. \quad (17)$$

Equation (16) represents the *kinematic coupling condition* and describes the continuity of fluid and structure velocities on $\Gamma_{wall}(t)$. The *dynamic coupling condition* is represented by equation (6) that describes the balance of forces and the continuity of fluid and structure stresses.

2.1 WEAK FORMULATION OF THE MODEL

Before presenting the splitting algorithm and analyzing its stability let us write down the weak formulation of the model (2), (5)-(16). Let the test functions \mathbf{v} and q belong to the following spaces

$$V := \{\mathbf{v} = (v_1, v_2) \in (W^{1,q}(\Omega_t))^2; v_1|_{\Gamma_{wall}} = 0, v_2|_{\Gamma_{sym}} = 0, v_2|_{x_2=0} = 0\}, \quad \text{a. e. } t \in I, \quad (18)$$

$$Q := L^2(\Omega_t), \quad \text{a. e. } t \in I, \quad (19)$$

respectively. Then we are looking for functions

$$\mathbf{u} \in L^q(0, T; W^{1,q}(\Omega_t)) \cap L^\infty(0, T; L^2(\Omega_t)), \quad (20)$$

$$\eta \in H^1(0, T; H_0^1(0, L)) \cap W^{1,\infty}(0, T; L^2(0, L)), \quad (21)$$

such that for a.e. $t \in (0, T)$

$$\begin{aligned} & \int_{\Omega_t} \mathbf{v} \cdot \frac{\mathcal{D}^A \mathbf{u}}{\mathcal{D}t} \, d\omega + \frac{2}{\rho_f} \int_{\Omega_t} \mu(|\mathbf{D}(\mathbf{u})|) \mathbf{D}(\mathbf{u}) : \mathbf{D}(\mathbf{v}) \, d\omega - \frac{1}{\rho_f} \int_{\Omega_t} p \, \nabla \cdot \mathbf{v} \, d\omega + \int_{\Omega_t} \mathbf{v} \cdot [(\mathbf{u} - \mathbf{w}) \cdot \nabla \mathbf{u}] \, d\omega \\ &= \frac{1}{\rho_f} \int_{\Omega_t} \mathbf{v} \cdot \mathbf{f} \, d\omega - \frac{\rho_s h}{\rho_f} \int_{\Gamma_{wall}^0} \left(\frac{\partial^2 \eta}{\partial t^2} - a \frac{\partial^2 \eta}{\partial x_1^2} + b \eta - c \frac{\partial^3 \eta}{\partial t \partial x_1^2} \right) v_2|_{\Gamma_{wall}^0} \, dl_0 + a \frac{\rho_s h}{\rho_f} \int_{\Gamma_{wall}^0} \frac{\partial^2 R_0}{\partial x_1^2} v_2|_{\Gamma_{wall}^0} \, dl_0 \\ & - \frac{1}{\rho_f} \int_{\Gamma_{wall}} \frac{P_{ext} v_2}{\sqrt{1 + (\partial_{x_1} R)^2}} \, dl + \int_{\Gamma_{in}} \left(\frac{1}{\rho_f} P_{in} - \frac{1}{2} |\mathbf{u}|^2 \right) v_1 \, dx_2 - \int_{\Gamma_{out}} \left(\frac{1}{\rho_f} P_{out} - \frac{1}{2} |\mathbf{u}|^2 \right) v_1 \, dx_2, \quad \forall \mathbf{v} \in V, \\ & \int_{\Omega_t} \nabla \cdot \mathbf{u} \, q \, d\omega = 0, \quad \forall q \in Q, \end{aligned} \quad (22)$$

where dl and dl_0 denote the lengths of elements from Γ_{wall} and Γ_{wall}^0 along the x_1 -direction, respectively. Here the boundary integral $\int_{\partial\Omega_t} (\mathbf{T} \mathbf{v}) \cdot \mathbf{n} \, dS$ has been replaced by the given boundary data and the structure equation. More detail on the derivation of boundary terms, in particular using the test function $\mathbf{v} = \mathbf{u}$, can be found in the Appendix A. The weak formulation (22) will be a base for the stability analysis in the next chapter. The well-posedness of this coupled fluid-structure interaction problem has been studied in [31] for $q \geq 2$, cf. (2). Note that the non-Newtonian polynomial growth condition on μ , in particular the power law exponent q , influences also suitable functional spaces [17].

3 STABILITY ANALYSIS

One of the most important numerical difficulties arising in analysis of conservation laws is their nonlinear character. Another peculiarity that occurs especially in the modelling of blood flow is the comparable magnitude of blood density with the one of vessel's tissue. This in contrast to other mechanical applications commonly used in loosely coupled schemes exhibits instabilities due to the artificial added mass effect, cf. [14, 18, 19]. As a consequence even small perturbations may cause large numerical instabilities. For that reason the choice of a suitable coupling strategy plays an important role and various approaches have been proposed in literature [4, 11, 14, 18, 19, 53].

In this paper we will derive an efficient loosely-coupled fluid-structure interaction algorithm using an operator splitting technique. Here we are inspired by the paper of Guidoboni et al. [27]. Similarly as in the earlier work of Nobile and Vergara [40] our scheme is based on computing the fluid and structure equation just once per time step. In [40] the structure equation is embedded into the fluid equation as a generalized Robin boundary condition. On the other hand, in the kinematic splitting algorithm, studied in our paper, the coupled fluid-structure interaction problem is split following the underlying physics into the hydrodynamic (parabolic) and elastic (hyperbolic) part. It is just a part of the structure equation, the parabolic part with the viscoelastic term, that is used as the generalized Robin boundary condition in the fluid equation. The rest of the structure equation, the elastic part, is approximated by a suitable numerical scheme; we have used the second order Newmark method. We would also like to point out that our analysis generalizes the result from [27]: we take explicitly the domain movement into account, apply the ALE formulation and point out the role of geometric conservation law. We analyse two possible time discretizations of the convective term with a domain velocity. In the case that the explicit discretization is used we derive the corresponding stability condition for the time step. However, if the midpoint rule has been used in order to approximate the domain velocity convective term, then the kinematic splitting

algorithm is unconditionally stable. Using the energy estimates technique and the geometric conservation law analogous stability results for implicit or semi-implicit fully coupled schemes have been obtained in [39]. We point out again that in our kinematic splitting algorithm no subiterations between fluid and structure are needed. More precisely it means, that the position of moving wall is treated in an explicit way and the fluid equation is solved in the domain computed at the old time step. Fluid and structure are coupled just through the kinematic boundary condition, it is the term $\xi^{n+1/2}$ that represents the communication between operators A and B, cf. (28), (29), (30). Finally, let us also recall that we will consider a non-Newtonian shear-dependent model for the fluid and thus our nonlinearities arise not only through the geometry and the convective term but also in the viscous fluid term.

3.1 KINEMATIC SPLITTING

The operator splitting approach is based on the kinematic coupling condition (16). We define the operator A that includes the fluid solver and the viscoelastic part of structure equation

$$\mathbf{Operator\ A\ (hydrodynamic)} \left\{ \begin{array}{l} \text{fluid solver } (\mathbf{u}, p), \\ \xi := u_2|_{\Gamma_{wall}}, \\ \frac{\partial \xi}{\partial t} = c \frac{\partial^2 \xi}{\partial x_1^2} + H(\mathbf{u}, p) \end{array} \right. \quad (23)$$

and the operator B for the purely elastic load of structure

$$\mathbf{Operator\ B\ (elastic)} \left\{ \begin{array}{l} \frac{\partial \eta}{\partial t} = \xi, \\ \frac{\partial \xi}{\partial t} = a \frac{\partial^2 \eta}{\partial x_1^2} - b\eta + G(R_0), \end{array} \right. \quad (24)$$

where $G(R_0) := a \frac{\partial^2 R_0}{\partial x_1^2}$. Since the structure equation has been obtained under the assumption $\partial_{x_1} \eta(x_1, t) \ll 1$ (linear elasticity) we will approximate $\sqrt{1 + (\partial_{x_1} R)^2} \approx \sqrt{1 + (\partial_{x_1} (R_0))^2}$ in the term with P_{ext} .

We derive an energy estimate for the discretized problem (23)-(24). The coupling condition allows us to rewrite the hydrodynamic part of structure equation in the terms of wall velocity ξ . This is a suitable form for numerical simulations, cf. Section 4. Time discretization of our problem is done as follows: we start with the fluid equation in Ω^n (i.e. Ω_t for $t = t^n$). We compute new velocities $\tilde{\mathbf{u}}^{n+1}$, pressures \tilde{p}^{n+1} and the wall velocity $\xi^{n+1/2}$. Herewith the computation of the operator A (23) is completed and we proceed with the operator B. From the elastic load of structure new wall displacement η^{n+1} and new wall velocity ξ^{n+1} are computed. Knowing η^{n+1} the geometry is updated from Ω^n to Ω^{n+1} and new values of fluid velocity \mathbf{u}^{n+1} and pressure p^{n+1} are mapped onto Ω^{n+1} . It means

$$\tilde{\mathbf{u}}^{n+1} := \mathbf{u}^{n+1} \circ \mathcal{A}_{t^{n+1}} \circ \mathcal{A}_{t^n}^{-1} \quad \text{and} \quad \tilde{p}^{n+1} := p^{n+1} \circ \mathcal{A}_{t^{n+1}} \circ \mathcal{A}_{t^n}^{-1}, \quad (25)$$

where \mathcal{A}_{t^n} is the ALE mapping from a reference domain Ω_{ref} onto Ω^n . Thus $\tilde{\mathbf{u}}^{n+1}$, \tilde{p}^{n+1} are the solutions computed on Ω^n at new time level t^{n+1} . The final solution at the time level t^{n+1} on Ω^{n+1} is denoted by \mathbf{u}^{n+1} , p^{n+1} . Moreover, we will use the notation $\mathcal{A}_{t^n, t^{n+1}} := \mathcal{A}_{t^{n+1}} \circ \mathcal{A}_{t^n}^{-1}$ for the ALE mapping between two time levels t^n and t^{n+1} . In order to update the domain Ω^n we need to define the grid velocity \mathbf{w} . First, we set $\mathbf{w}|_{\Gamma_{wall}} \cdot \mathbf{e}_r = \xi^{n+1}$. In order to define grid velocity also inside Ω^n we may solve an auxiliary problem, e.g., cf. [21]. For $\mathbf{x}^n \in \Omega^n$ and $\Theta^{n+1} := (0, \eta^{n+1})$

$$\begin{aligned} \Delta_Y \mathbf{x} &= 0 \quad \text{for } Y \in \Omega_{ref}, \\ \mathbf{x} &:= \mathcal{A}_t(\mathbf{Y}) = \mathbf{x}^n + \Theta^{n+1} \quad \text{on } \Gamma_{wall}^{n+1}, \\ \mathbf{x} &= \mathbf{x}^n \quad \text{on } \partial\Omega^{n+1} \setminus \Gamma_{wall}^{n+1}. \end{aligned}$$

Consequently, we get $\mathbf{x}^{n+1} = \mathbf{x}$ and compute the grid velocity as $\mathbf{w}^{n+1} := \frac{\mathbf{x}^{n+1} - \mathbf{x}^n}{t^{n+1} - t^n}$. Provided that the weak solution of our FSI problem is enough regular the above auxiliary problem can be approximated as in [21] with higher order finite elements, so that the (discrete) ALE mapping and correspondingly the grid velocity satisfy the required regularity; in particular $\mathbf{w}^n \in W^{1,\infty}(\Omega^n)$, see also Remark 3.1. In order to define $\mathbf{x}(t)$, $t \in (t^n, t^{n+1}]$ we can use the linear interpolation in time

$$\mathbf{x}(t) = \mathcal{A}_t(\mathbf{Y}) := \frac{t - t^n}{t^{n+1} - t^n} \mathcal{A}_{t^{n+1}}(\mathbf{Y}) + \frac{t^{n+1} - t}{t^{n+1} - t^n} \mathcal{A}_{t^n}(\mathbf{Y}), \quad t \in (t^n, t^{n+1}]. \quad (26)$$

Now, we can define $\mathbf{w}(t)$ as

$$\mathbf{w}(\mathbf{x}(t), t) = \frac{\mathbf{x}(t) - \mathbf{x}^n}{t - t^n}. \quad (27)$$

In what follows our aim is to derive an energy estimate for the operator splitting scheme (23)-(24). To this end we derive firstly a suitable semi-discrete scheme and approximate the time derivative in the operator A by the backward Euler method. The first order Euler scheme has been chosen for convenience. Analysis for the second order schemes, e.g., the Crank-Nicolson scheme, would be analogous. Now integrating the fluid equation over Ω^n , testing it with $\tilde{\mathbf{u}}^{n+1}$ and applying a part of the dynamic boundary condition from (23)₃ on Γ_{wall}^n yield, cf. (22),

$$\begin{aligned} & \int_{\Omega^n} \tilde{\mathbf{u}}^{n+1} \cdot \frac{\tilde{\mathbf{u}}^{n+1} - \mathbf{u}^n}{\Delta t} \, d\omega + \frac{2}{\rho_f} \int_{\Omega^n} \mu(|\mathbf{D}(\tilde{\mathbf{u}}^{n+1})|) \mathbf{D}(\tilde{\mathbf{u}}^{n+1}) : \mathbf{D}(\tilde{\mathbf{u}}^{n+1}) \, d\omega + \frac{1}{2} \int_{\Omega^n} |\tilde{\mathbf{u}}^{n+1}|^2 \nabla \cdot \mathbf{w}^n \, d\omega \\ &= -\frac{\rho_s h}{\rho_f} \int_{\Gamma_{wall}^0} \left[\frac{\xi^{n+\frac{1}{2}} - \xi^n}{\Delta t} \right] \xi^{n+\frac{1}{2}} \, dl_0 - \frac{\rho_s h c}{\rho_f} \int_{\Gamma_{wall}^0} \left[\frac{\partial \xi^{n+\frac{1}{2}}}{\partial x_1} \right]^2 \, dl_0 - \frac{1}{\rho_f} \int_{\Gamma_{wall}^n} \frac{P_{ext}(t^{n+1}) \tilde{u}_2^{n+1}}{\sqrt{1 + (\partial_{x_1} R_0)^2}} \, dl \\ &+ \frac{1}{\rho_f} \int_0^{R_0(0)} P_{in}(t^{n+1}) \tilde{u}_1^{n+1}|_{x_1=0} \, dx_2 - \frac{1}{\rho_f} \int_0^{R_0(L)} P_{out}(t^{n+1}) \tilde{u}_1^{n+1}|_{x_1=L} \, dx_2 + \frac{1}{\rho_f} \int_{\Omega^n} \tilde{\mathbf{u}}^{n+1} \cdot \mathbf{f}^{n+1} \, d\omega, \quad (28) \end{aligned}$$

where $\Delta t = t^{n+1} - t^n$ denotes the time step. We consider here only semi-discrete scheme having space continuous representation. To simplify the matter we assume that we have divergence-free velocities on Ω^n . In our numerical scheme this is realized through the artificial compressibility approach. More precisely the solenoidal condition is replaced by

$$-\varepsilon \Delta \tilde{p}^{n+1} + \nabla \cdot \tilde{\mathbf{u}}^{n+1} = 0 \text{ on } \Omega^n.$$

Here ε is a small positive constant, $\varepsilon \approx \Delta h^2$, where Δh denotes the grid size. See also our recent theoretical work [31], where the artificial compressibility approach is used to show the existence of a weak solution and [45]. Another approach to deal with the div-free condition on moving domains has been used in the projection semi-implicit FSI scheme by Fernández, Gerbeau and Grandmont [18], where the pressure projection step (Chorin projection) is applied as an implicit coupling.

In what follows the operator B will be discretized in time via the Crank-Nicolson scheme, i.e.

$$\frac{\eta^{n+1} - \eta^n}{\Delta t} = \frac{1}{2} (\xi^{n+1} + \xi^{n+\frac{1}{2}}), \quad (29)$$

$$\frac{\xi^{n+1} - \xi^{n+\frac{1}{2}}}{\Delta t} = \frac{a}{2} (\eta_{x_1 x_1}^{n+1} + \eta_{x_1 x_1}^n) - \frac{b}{2} (\eta^{n+1} + \eta^n) + G(R_0). \quad (30)$$

Recall that the parameters a , b and c from (28) and (30) are defined in (9). The discrete scheme (29)-(30) is also reported in literature as the Newmark scheme. Next, we derive energy estimates for the operator A and the operator B, respectively.

3.2 ENERGY ESTIMATE - OPERATOR A

For each time step $t = t^{n+1}$ we look for an energy estimate of the non-conservative discrete weak formulation of the momentum equation (28). In order to control the energy of the operator A we firstly apply the Young inequality for the time-difference term

$$\int_{\Omega^n} \tilde{\mathbf{u}}^{n+1} \cdot \frac{\tilde{\mathbf{u}}^{n+1} - \mathbf{u}^n}{\Delta t} \, d\omega \geq \frac{1}{2\Delta t} \|\tilde{\mathbf{u}}^{n+1}\|_{L^2(\Omega^n)}^2 - \frac{1}{2\Delta t} \|\mathbf{u}^n\|_{L^2(\Omega^n)}^2. \quad (31)$$

Before estimating the viscous term, let us point out that for both shear-thinning viscosity function models, the Carreau and the Yeleswarapu, we have

$$\mu(|\mathbf{D}(\tilde{\mathbf{u}}^{n+1})|) \geq \mu_\infty$$

that yields the existence of a constant $C^* > 0$, such that

$$\frac{2}{\rho_f} \int_{\Omega^n} \mu(|\mathbf{D}(\tilde{\mathbf{u}}^{n+1})|) \mathbf{D}(\tilde{\mathbf{u}}^{n+1}) : \mathbf{D}(\tilde{\mathbf{u}}^{n+1}) \, d\omega \geq C^* \|\tilde{\mathbf{u}}^{n+1}\|_{W^{1,2}(\Omega^n)}^2. \quad (32)$$

Moreover, we have for the Carreau model, cf. [31], [36], Lemma 5.1.19,

$$\frac{2}{\rho_f} \int_{\Omega^n} \mu(|\mathbf{D}(\tilde{\mathbf{u}}^{n+1})|) \mathbf{D}(\tilde{\mathbf{u}}^{n+1}) : \mathbf{D}(\tilde{\mathbf{u}}^{n+1}) \, d\omega \geq C^* \|\tilde{\mathbf{u}}^{n+1}\|_{W^{1,q}(\Omega^n)}^q - \kappa C^*, \quad (33)$$

where $\kappa := 0$ for $q \geq 2$ and $\kappa = 1$ for $1 \leq q < 2$. For $q \geq 2$, see [36], we also have

$$\frac{2}{\rho_f} \int_{\Omega^n} \mu(|\mathbf{D}(\tilde{\mathbf{u}}^{n+1})|) \mathbf{D}(\tilde{\mathbf{u}}^{n+1}) : \mathbf{D}(\tilde{\mathbf{u}}^{n+1}) \, d\omega \geq C^* \|\tilde{\mathbf{u}}^{n+1}\|_{W^{1,q}(\Omega^n)}^q + C^* \|\tilde{\mathbf{u}}^{n+1}\|_{W^{1,2}(\Omega^n)}^2. \quad (34)$$

In what follows we will present a stability analysis for a polynomial growth model with the property (33). We use (33) instead of (34), because we are focused on the shear-thinning fluids. However, the analysis will be analogous for (32) and (34), too.

Third term in (28) contains the domain velocity function. We can estimate it in the following way

$$- \int_{\Omega^n} |\tilde{\mathbf{u}}^{n+1}|^2 \nabla \cdot \mathbf{w}^n \, d\omega \leq \alpha^n \|\tilde{\mathbf{u}}^{n+1}\|_{L^2(\Omega^n)}^2, \quad (35)$$

where $\alpha^n := \|\nabla \cdot \mathbf{w}^n\|_{L^\infty(\Omega^n)}$, cf. Remark 3.1.

Moreover, using the Young inequality we can bound from above the source term

$$\frac{1}{\rho_f} \int_{\Omega^n} \tilde{\mathbf{u}}^{n+1} \cdot \mathbf{f}^{n+1} \, d\omega \leq C_1 \varepsilon \|\tilde{\mathbf{u}}^{n+1}\|_{L^q(\Omega^n)}^q + \frac{C_2}{\varepsilon^{q'/q}} \|\mathbf{f}^{n+1}\|_{L^{q'}(\Omega^n)}^{q'}, \quad (36)$$

where $q' \geq 1$, such that $1/q + 1/q' = 1$ and C_1, C_2 are positive constants.

We estimate the boundary terms with a prescribed pressure contribution by the Young and the trace inequality as follows

$$\begin{aligned} \frac{1}{\rho_f} \int_0^{R_0(0)} P_{in}(t^{n+1}) \tilde{u}_1^{n+1}|_{x_1=0} \, dx_2 &\leq \frac{C_2}{\varepsilon_1^{q'/q}} \|P_{in}(t^{n+1})\|_{L^{q'}(\Gamma_{in})}^{q'} \\ &+ \varepsilon_1 C_1 C_1^{tr}(\Omega^n) \|\tilde{\mathbf{u}}^{n+1}\|_{W^{1,q}(\Omega^n)}^q, \end{aligned} \quad (37)$$

$$\begin{aligned} \frac{1}{\rho_f} \int_0^{R_0(L)} P_{out}(t^{n+1}) \tilde{u}_1^{n+1}|_{x_1=L} \, dx_2 &\leq \frac{C_2}{\varepsilon_2^{q'/q}} \|P_{out}(t^{n+1})\|_{L^{q'}(\Gamma_{out})}^{q'} \\ &+ \varepsilon_2 C_1 C_2^{tr}(\Omega^n) \|\tilde{\mathbf{u}}^{n+1}\|_{W^{1,q}(\Omega^n)}^q, \end{aligned} \quad (38)$$

$$\begin{aligned}
-\frac{1}{\rho_f} \int_{\Gamma_{wall}^n} \frac{P_{ext}(t^{n+1}) \tilde{u}_2^{n+1}}{\sqrt{1 + (\partial_{x_1} R_0)^2}} dl &\leq \frac{KC_2}{\varepsilon_3^{q'/q}} \|P_{ext}(t^{n+1})\|_{L^{q'}(\Gamma_{wall}^n)}^{q'} \\
&+ \varepsilon_3 C_1 C_3^{tr}(\Omega^n) \|\tilde{\mathbf{u}}^{n+1}\|_{W^{1,q}(\Omega^n)}^q,
\end{aligned} \tag{39}$$

where ε_i and $C_i^{tr}(\Omega^{n+1})$, $i \in \{1, 2, 3\}$, are positive constants and $K := \left\| [1 + (\partial_{x_1} R_0)^2]^{-1/2} \right\|_{L^\infty(\Gamma_{wall}^n)}$.

Further estimates on Γ_{wall}^0 are obtained using the Young inequality

$$-\int_{\Gamma_{wall}^0} \frac{\xi^{n+\frac{1}{2}} - \xi^n}{\Delta t} \xi^{n+\frac{1}{2}} dl_0 \leq -\frac{1}{2\Delta t} \|\xi^{n+\frac{1}{2}}\|_{L^2(\Gamma_{wall}^0)}^2 + \frac{1}{2\Delta t} \|\xi^n\|_{L^2(\Gamma_{wall}^0)}^2, \tag{40}$$

$$-c \int_{\Gamma_{wall}^0} \left[\frac{\partial \xi^{n+\frac{1}{2}}}{\partial x_1} \right]^2 dl_0 = -c \|\xi_{x_1}^{n+\frac{1}{2}}\|_{L^2(\Gamma_{wall}^0)}^2. \tag{41}$$

Let $C^{tr} := C_1^{tr} = C_2^{tr} = C_3^{tr}$ and $\varepsilon := \varepsilon_1 = \varepsilon_2 = \varepsilon_3/K$. Inserting (31)-(41) into (28) we obtain

$$\begin{aligned}
&\frac{1}{2\Delta t} \left[\|\tilde{\mathbf{u}}^{n+1}\|_{L^2(\Omega^n)}^2 - \|\mathbf{u}^n\|_{L^2(\Omega^n)}^2 \right] + C^* \left[\|\tilde{\mathbf{u}}^{n+1}\|_{W^{1,q}(\Omega^n)}^q - \kappa \right] \\
&+ \frac{\rho_s h}{\rho_f} \left[\frac{1}{2\Delta t} \|\xi^{n+\frac{1}{2}}\|_{L^2(\Gamma_{wall}^0)}^2 - \frac{1}{2\Delta t} \|\xi^n\|_{L^2(\Gamma_{wall}^0)}^2 + c \|\xi_{x_1}^{n+\frac{1}{2}}\|_{L^2(\Gamma_{wall}^0)}^2 \right] \\
&\leq \frac{\alpha^n}{2} \|\tilde{\mathbf{u}}^{n+1}\|_{L^2(\Omega^n)}^2 + \varepsilon C_1 \|\tilde{\mathbf{u}}^{n+1}\|_{L^q(\Omega^n)}^q + 3\varepsilon C_1 C^{tr}(\Omega^n) \|\tilde{\mathbf{u}}^{n+1}\|_{W^{1,q}(\Omega^n)}^q + \frac{C_2}{\varepsilon^{q'/q}} \text{RHS}^{n+1},
\end{aligned} \tag{42}$$

where

$$\text{RHS}^{n+1} := \|P_{in}(t^{n+1})\|_{L^{q'}(\Gamma_{in})}^{q'} + \|P_{out}(t^{n+1})\|_{L^{q'}(\Gamma_{out})}^{q'} + \|P_{ext}(t^{n+1})\|_{L^{q'}(\Gamma_{wall}^n)}^{q'} + \|\mathbf{f}^{n+1}\|_{L^{q'}(\Omega^{n+1})}^{q'}. \tag{43}$$

Moreover, let $\varepsilon > 0$ be sufficiently small, such that $\varepsilon < C^*/(2C_1(1 + 3C^{tr}))$. Then it holds

$$C^* \|\tilde{\mathbf{u}}^{n+1}\|_{W^{1,q}(\Omega^n)}^q - \varepsilon C_1 \|\tilde{\mathbf{u}}^{n+1}\|_{L^q(\Omega^n)}^q - 3\varepsilon C_1 C^{tr}(\Omega_t) \|\tilde{\mathbf{u}}^{n+1}\|_{W^{1,q}(\Omega^n)}^q \geq \frac{C^*}{2} \|\tilde{\mathbf{u}}^{n+1}\|_{W^{1,q}(\Omega^n)}^q. \tag{44}$$

Multiplying (42) by $2\Delta t$ and using the estimate (44) we have

$$\begin{aligned}
&\|\tilde{\mathbf{u}}^{n+1}\|_{L^2(\Omega^n)}^2 + C^* \Delta t \|\tilde{\mathbf{u}}^{n+1}\|_{W^{1,q}(\Omega^n)}^q \\
&+ \frac{\rho_s h}{\rho_f} \left[\|\xi^{n+\frac{1}{2}}\|_{L^2(\Gamma_{wall}^0)}^2 - \|\xi^n\|_{L^2(\Gamma_{wall}^0)}^2 + 2\Delta t c \|\xi_{x_1}^{n+\frac{1}{2}}\|_{L^2(\Gamma_{wall}^0)}^2 \right] \\
&\leq \|\mathbf{u}^n\|_{L^2(\Omega^n)}^2 + \alpha^n \Delta t \|\tilde{\mathbf{u}}^{n+1}\|_{L^2(\Omega^n)}^2 + \frac{2\Delta t C_2}{\varepsilon^{q'/q}} \text{RHS}^{n+1} + 2C^* \kappa \Delta t.
\end{aligned} \tag{45}$$

The basic idea of implementation of time dependent domain requires that a numerical scheme should reproduce a constant solution, cf. [34, 39]. Indeed, as a consequence of the Reynolds transport theorem we obtain that the so-called **Geometric Conservation Law** (GCL) holds true, i.e.

$$\int_{\Omega^{n+1}} d\omega - \int_{\Omega^n} d\omega = \int_{t^n}^{t^{n+1}} \int_{\Omega_t} \nabla \cdot \mathbf{w} d\omega dt, \tag{46}$$

where $\mathbf{w}(\mathbf{x}, t)$, $t \in (t^n, t^{n+1}]$ is defined in (27). Following this idea we obtain analogously as in [21, 40]

$$\|\mathbf{u}^{n+1}\|_{L^2(\Omega^{n+1})}^2 - \|\tilde{\mathbf{u}}^{n+1}\|_{L^2(\Omega^n)}^2 = \int_{t^n}^{t^{n+1}} \int_{\Omega_t} |\tilde{\mathbf{u}}|^2 \nabla \cdot \mathbf{w} d\omega dt. \tag{47}$$

Here $\tilde{\mathbf{u}} := \mathbf{u}^{n+1} \circ \mathcal{A}_{t,t^{n+1}}$. The relation (47) can be again derived from the Reynold transport theorem using the fact that $\mathbf{u}^{n+1}(\mathbf{x}) = \sum_{i=1}^{\infty} u_i^{n+1} \psi_i(\mathbf{x})$, $\mathbf{x} \in \Omega^{n+1}$, where $\psi_i(\mathbf{x}) = \psi_i(\mathcal{A}_t(\mathbf{Y}))$ and $\psi_i(\mathbf{Y})$, $i \in \mathbb{N}$

are the basis functions from $W^{1,q}(\Omega_{ref})$. Denoting J_A the determinant of the Jacobian matrix of the ALE mapping the right hand side of (47) can be further estimated in the following way

$$\begin{aligned} \int_{t^n}^{t^{n+1}} \int_{\Omega_t} |\tilde{\mathbf{u}}|^2 \nabla \cdot \mathbf{w} \, d\omega \, dt &= \int_{t^n}^{t^{n+1}} \int_{\Omega^n} |\mathbf{u}^n|^2 \nabla \cdot \mathbf{w} |J_{A_{t^n, t^{n+1}}}^{-1}(t)| \, d\omega \, dt \\ &\leq \int_{t^n}^{t^{n+1}} \|\nabla \cdot \mathbf{w} |J_{A_{t^n, t^{n+1}}}^{-1}|\|_{L^\infty(\Omega^n)} \int_{\Omega^n} |\mathbf{u}^n|^2 \, d\omega \, dt \leq \beta^n \Delta t \|\mathbf{u}^n\|_{L^2(\Omega^n)}^2, \end{aligned} \quad (48)$$

where $\beta^n := \sup_{t \in (t^n, t^{n+1})} \left\{ \|\nabla \cdot \mathbf{w} |J_{A_{t^n, t^{n+1}}}^{-1}|\|_{L^\infty(\Omega^n)} \right\}$. Inserting (48) to (47) we obtain the estimate

$$\|\tilde{\mathbf{u}}^{n+1}\|_{L^2(\Omega^n)}^2 \geq \|\mathbf{u}^{n+1}\|_{L^2(\Omega^{n+1})}^2 - \beta^n \Delta t \|\mathbf{u}^n\|_{L^2(\Omega^n)}^2. \quad (49)$$

Moreover, using the GCL condition (47) we can rewrite the second term on the right hand side of (45) in the following way

$$\alpha^n \Delta t \|\tilde{\mathbf{u}}^{n+1}\|_{L^2(\Omega^n)}^2 \leq \alpha^n \Delta t \|\mathbf{u}^{n+1}\|_{L^2(\Omega^{n+1})}^2 + \alpha^n \beta^n (\Delta t)^2 \|\mathbf{u}^n\|_{L^2(\Omega^n)}^2. \quad (50)$$

Finally, using the inequalities (49) and (50) we can rewrite (45) as follows

$$\begin{aligned} &\|\mathbf{u}^{n+1}\|_{L^2(\Omega^{n+1})}^2 - \|\mathbf{u}^n\|_{L^2(\Omega^n)}^2 + C^* \Delta t \|\tilde{\mathbf{u}}^{n+1}\|_{W^{1,q}(\Omega^n)}^q \\ &+ \frac{\rho_s h}{\rho_f} \left[\|\xi^{n+\frac{1}{2}}\|_{L^2(\Gamma_{wall}^0)}^2 - \|\xi^n\|_{L^2(\Gamma_{wall}^0)}^2 + 2\Delta t c \|\xi_{x_1}^{n+\frac{1}{2}}\|_{L^2(\Gamma_{wall}^0)}^2 \right] \\ &\leq \beta^n \Delta t (1 + \alpha^n \Delta t) \|\mathbf{u}^n\|_{L^2(\Omega^n)}^2 + \alpha^n \Delta t \|\mathbf{u}^{n+1}\|_{L^2(\Omega^{n+1})}^2 \\ &+ \frac{2\Delta t C_2}{\varepsilon^{q'/q}} \text{RHS}^{n+1} + 2C^* \kappa \Delta t. \end{aligned} \quad (51)$$

Summing (51) for the first $n+1$ time steps we obtain the following estimate for the operator A

$$\begin{aligned} &\|\mathbf{u}^{n+1}\|_{L^2(\Omega^{n+1})}^2 + C^* \Delta t \sum_{i=0}^n \|\tilde{\mathbf{u}}^{i+1}\|_{W^{1,q}(\Omega^i)}^q \\ &+ \frac{\rho_s h}{\rho_f} \sum_{i=0}^n \left[\|\xi^{i+\frac{1}{2}}\|_{L^2(\Gamma_{wall}^0)}^2 - \|\xi^i\|_{L^2(\Gamma_{wall}^0)}^2 + 2\Delta t c \|\xi_{x_1}^{i+\frac{1}{2}}\|_{L^2(\Gamma_{wall}^0)}^2 \right] \\ &\leq \left[1 + \Delta t \beta^0 + (\Delta t)^2 \alpha^0 \beta^0 \right] \|\mathbf{u}^0\|_{L^2(\Omega_{ref})}^2 + \Delta t \sum_{i=1}^{n+1} \left[\beta^i (1 + \alpha^i \Delta t) + \alpha^{i-1} \right] \|\mathbf{u}^i\|_{L^2(\Omega^i)}^2 \\ &+ \frac{2\Delta t C_2}{\varepsilon^{q'/q}} \sum_{i=1}^{n+1} \text{RHS}^i + 2C^* \kappa T. \end{aligned} \quad (52)$$

Remark 3.1 As pointed out in Section 2 we assume that $\mathcal{A}_t \in W^{1,\infty}(\Omega_{ref})$, see also [21, 39]. This assumption also implies that $\mathbf{w}^n \in W^{1,q}(\Omega^n)$. Now, in order to guarantee that the solution of the harmonic extension problem $\mathbf{x}(t) = \mathcal{A}_t(\mathbf{Y}) \in W^{1,\infty}(\Omega_{ref})$ we need to assume the regularity of the domain Ω_{ref} as well as of the solution η of structure equation, see also [22] for discussions on the regularity of several structural models. In our recent theoretical work [31] we were able to show that $\eta \in H^1(0, T; H_0^2(0, L))$ provided that a higher order viscoelastic term $\frac{\partial^5 \eta}{\partial t \partial^4 x}$ was added. Under the assumption that the domain Ω_{ref} is enough regular we would obtain that \mathbf{w}^n has the desired regularity. The question of the regularity of the weak solution of (22) is still open.

3.3 ENERGY ESTIMATE - OPERATOR B

The goal of this section is to find an energy estimate for the semi-discrete scheme (29)-(30). Multiplying the equation (29) by $b(\eta^{n+1} + \eta^n)$ and the equation (30) by $(\xi^{n+1} + \xi^{n+\frac{1}{2}})$ we obtain

$$b \frac{(\eta^{n+1})^2 - (\eta^n)^2}{\Delta t} = \frac{b}{2} (\xi^{n+1} + \xi^{n+\frac{1}{2}}) (\eta^{n+1} + \eta^n), \quad (53)$$

$$\begin{aligned} \frac{(\xi^{n+1})^2 - (\xi^{n+\frac{1}{2}})^2}{\Delta t} &= \frac{a}{2} (\eta_{x_1 x_1}^{n+1} + \eta_{x_1 x_1}^n) (\xi^{n+1} + \xi^{n+\frac{1}{2}}) - \frac{b}{2} (\eta^{n+1} + \eta^n) (\xi^{n+1} + \xi^{n+\frac{1}{2}}) \\ &+ G(R_0) (\xi^{n+1} + \xi^{n+\frac{1}{2}}). \end{aligned} \quad (54)$$

Summing (53) and (54), rewriting the left hand side and integrating over Γ_{wall}^0 we obtain the following equation

$$\begin{aligned} &\int_{\Gamma_{wall}^0} \left(b \frac{(\eta^{n+1})^2 - (\eta^n)^2}{\Delta t} + \frac{(\xi^{n+1})^2 - (\xi^n)^2}{\Delta t} + \frac{(\xi^n)^2 - (\xi^{n+\frac{1}{2}})^2}{\Delta t} \right) dl_0 \\ &= \int_{\Gamma_{wall}^0} \frac{a}{2} (\eta_{x_1 x_1}^{n+1} + \eta_{x_1 x_1}^n) (\xi^{n+1} + \xi^{n+\frac{1}{2}}) dl_0 + \int_{\Gamma_{wall}^0} G(R_0) (\xi^{n+1} + \xi^{n+\frac{1}{2}}) dl_0. \end{aligned} \quad (55)$$

For the sake of simplicity let us assume that we have zero boundary conditions for η , see (15). Then using (29) and integration by parts the right hand side of (55) reads as follows

$$\frac{a}{2} \int_{\Gamma_{wall}^0} (\eta_{x_1 x_1}^{n+1} + \eta_{x_1 x_1}^n) (\xi^{n+1} + \xi^{n+\frac{1}{2}}) dl_0 = -a \int_{\Gamma_{wall}^0} \frac{(\eta_{x_1}^{n+1})^2 - (\eta_{x_1}^n)^2}{\Delta t} dl_0, \quad (56)$$

$$\int_{\Gamma_{wall}^0} G(R_0) (\xi^{n+1} + \xi^{n+\frac{1}{2}}) dl_0 = \frac{2}{\Delta t} \int_{\Gamma_{wall}^0} G(R_0) (\eta^{n+1} - \eta^n) dl_0. \quad (57)$$

Inserting (56) and (57) into (55) and summing from 0 to n we obtain

$$\begin{aligned} &a \|\eta_{x_1}^{n+1}\|_{L^2(\Gamma_{wall}^0)}^2 + b \|\eta^{n+1}\|_{L^2(\Gamma_{wall}^0)}^2 + \|\xi^{n+1}\|_{L^2(\Gamma_{wall}^0)}^2 \\ &\leq a \|\eta_{x_1}^0\|_{L^2(\Gamma_{wall}^0)}^2 + b \|\eta^0\|_{L^2(\Gamma_{wall}^0)}^2 + \|\xi^0\|_{L^2(\Gamma_{wall}^0)}^2 \\ &+ \sum_{i=0}^n \left(\|\xi^{i+\frac{1}{2}}\|_{L^2(\Gamma_{wall}^0)}^2 - \|\xi^i\|_{L^2(\Gamma_{wall}^0)}^2 \right) + \int_{\Gamma_{wall}^0} 2G(R_0) (\eta^{n+1} - \eta^0) dl_0. \end{aligned} \quad (58)$$

Recall that $G(R_0) := a \frac{\partial^2 R_0}{\partial x_1^2}$. Now, for small positive numbers δ_1, δ_2 the integral in (58) can be estimates as follows

$$\int_{\Gamma_{wall}^0} 2G(R_0) (\eta^{n+1} - \eta^0) dl_0 \leq 2aL \left[\frac{|\Gamma_{wall}^0|}{4 \delta_1} + \frac{|\Gamma_{wall}^0|}{4 \delta_2} + \delta_1 \|\eta^{n+1}\|_{L^2(\Gamma_{wall}^0)}^2 + \delta_2 \|\eta^0\|_{L^2(\Gamma_{wall}^0)}^2 \right],$$

where $L := \left\| \frac{\partial^2 R_0}{\partial x_1^2} \right\|_{L^\infty(\Gamma_{wall}^0)}$. Let $\delta_1 = \delta_2 =: \delta$ be sufficiently small such that $aL\delta \leq b/4$, then

$$\int_{\Gamma_{wall}^0} 2G(R_0) (\eta^{n+1} - \eta^0) dl_0 \leq \frac{aL|\Gamma_{wall}^0|}{\delta} + \frac{b}{2} \left[\|\eta^{n+1}\|_{L^2(\Gamma_{wall}^0)}^2 + \|\eta^0\|_{L^2(\Gamma_{wall}^0)}^2 \right]. \quad (59)$$

Inserting (59) into (58) we obtain an estimate of the operator B

$$\begin{aligned} &a \|\eta_{x_1}^{n+1}\|_{L^2(\Gamma_{wall}^0)}^2 + \frac{b}{2} \|\eta^{n+1}\|_{L^2(\Gamma_{wall}^0)}^2 + \|\xi^{n+1}\|_{L^2(\Gamma_{wall}^0)}^2 \\ &\leq a \|\eta_{x_1}^0\|_{L^2(\Gamma_{wall}^0)}^2 + \frac{3b}{2} \|\eta^0\|_{L^2(\Gamma_{wall}^0)}^2 + \|\xi^0\|_{L^2(\Gamma_{wall}^0)}^2 \\ &+ \sum_{i=0}^n \left(\|\xi^{i+\frac{1}{2}}\|_{L^2(\Gamma_{wall}^0)}^2 - \|\xi^i\|_{L^2(\Gamma_{wall}^0)}^2 \right) + \frac{aL|\Gamma_{wall}^0|}{\delta}. \end{aligned} \quad (60)$$

Note that in our model we have $\eta^0 = 0$ and $\xi^0 = u_2^0|_{\Gamma_{wall}}$.

3.4 FINAL ENERGY ESTIMATE

Combining the estimates for the operator A, cf. (52), with the operator B, cf. (60), we obtain

$$\begin{aligned}
& \|\mathbf{u}^{n+1}\|_{L^2(\Omega^{n+1})}^2 + \frac{\rho_s h}{\rho_f} \left[a \|\eta_{x_1}^{n+1}\|_{L^2(\Gamma_{wall}^0)}^2 + \frac{b}{2} \|\eta^{n+1}\|_{L^2(\Gamma_{wall}^0)}^2 + \|\xi^{n+1}\|_{L^2(\Gamma_{wall}^0)}^2 \right] \\
& + C^* \Delta t \sum_{i=0}^n \|\tilde{\mathbf{u}}^{i+1}\|_{W^{1,q}(\Omega^i)}^q + \frac{2\rho_s h c}{\rho_f} \Delta t \sum_{i=0}^n \|\xi_{x_1}^{i+\frac{1}{2}}\|_{L^2(\Gamma_{wall}^0)}^2 \\
& \leq \|\mathbf{u}^0\|_{L^2(\Omega^0)}^2 + \frac{\rho_s h}{\rho_f} \left[a \|\eta_{x_1}^0\|_{L^2(\Gamma_{wall}^0)}^2 + \frac{b}{2} \|\eta^0\|_{L^2(\Gamma_{wall}^0)}^2 + \|\xi^0\|_{L^2(\Gamma_{wall}^0)}^2 \right] \\
& + \left[\Delta t \beta^0 + (\Delta t)^2 \alpha^0 \beta^0 \right] \|\mathbf{u}^0\|_{L^2(\Omega_{ref})}^2 + \frac{\rho_s h b}{\rho_f} \|\eta^0\|_{L^2(\Gamma_{wall}^0)}^2 + 2C^* \kappa T \\
& + \Delta t \sum_{i=1}^{n+1} \left[\beta^i (1 + \alpha^i \Delta t) + \alpha^{i-1} \right] \|\mathbf{u}^i\|_{L^2(\Omega^i)}^2 + \frac{2\Delta t C_2}{\varepsilon^{q'/q}} \sum_{i=1}^{n+1} \text{RHS}^i + \frac{\rho_s h a}{\rho_f} \frac{L|\Gamma_{wall}^0|}{\delta}. \tag{61}
\end{aligned}$$

Let us denote

$$\begin{aligned}
E^i & := \|\mathbf{u}^i\|_{L^2(\Omega^i)}^2 + \frac{\rho_s h}{\rho_f} \left[a \|\eta_{x_1}^i\|_{L^2(\Gamma_{wall}^0)}^2 + \frac{b}{2} \|\eta^i\|_{L^2(\Gamma_{wall}^0)}^2 + \|\xi^i\|_{L^2(\Gamma_{wall}^0)}^2 \right], \\
G^i & := C^* \|\tilde{\mathbf{u}}^i\|_{W^{1,q}(\Omega^{i-1})}^q + \frac{2\rho_s h c}{\rho_f} \|\xi_{x_1}^{i-\frac{1}{2}}\|_{L^2(\Gamma_{wall}^0)}^2, \\
Q^0 & := \left[\Delta t \beta^0 + (\Delta t)^2 \alpha^0 \beta^0 \right] \|\mathbf{u}^0\|_{L^2(\Omega_{ref})}^2 + \frac{\rho_s h b}{\rho_f} \|\eta^0\|_{L^2(\Gamma_{wall}^0)}^2 + \frac{\rho_s h a}{\rho_f} \frac{L|\Gamma_{wall}^0|}{\delta} + 2C^* \kappa T, \\
P^i & := \frac{2C_2}{\varepsilon^{q'/q}} \text{RHS}^i,
\end{aligned}$$

where $i = 0, \dots, n+1$. Clearly, $\|\mathbf{u}^i\|_{L^2(\Omega^i)}^2 \leq E^i$ for all $i = 0, \dots, n+1$ and thus, we can rewrite (61) as follows

$$E^{n+1} + \Delta t \sum_{i=1}^{n+1} G^i \leq E^0 + Q^0 + \Delta t \sum_{i=1}^{n+1} P^i + \Delta t \sum_{i=1}^{n+1} \left[\beta^i (1 + \alpha^i \Delta t) + \alpha^{i-1} \right] E^i.$$

Finally, using the discrete Gronwall lemma, cf. Appendix B or e.g., [54], we obtain

$$E^{n+1} + \Delta t \sum_{i=1}^{n+1} G^i \leq \left[E^0 + Q^0 + \Delta t \sum_{i=1}^{n+1} P^i \right] \exp \left\{ \sum_{i=1}^{n+1} \frac{(\beta^i (1 + \alpha^i \Delta t) + \alpha^{i-1}) \Delta t}{1 - (\beta^i (1 + \alpha^i \Delta t) + \alpha^{i-1}) \Delta t} \right\}$$

with the following condition on the time step

$$\Delta t \leq \frac{1}{\beta^i (1 + \alpha^i \Delta t) + \alpha^{i-1}} \quad \text{for } i = 0, \dots, n+1. \tag{62}$$

We remind that

$$\alpha^n := \|\nabla \cdot \mathbf{w}^n\|_{L^\infty(\Omega^n)}, \quad \beta^n := \sup_{t \in (t^n, t^{n+1})} \left\{ \|\nabla \cdot \mathbf{w}|_{J_{A_{t^n, t}^{-1}}}\|_{L^\infty(\Omega^n)} \right\}.$$

We would like to point out that assuming a smooth grid movement the coefficients α^i and β^i are sufficiently small and thus condition (62) is not very restrictive. Indeed, our estimate is more general than those obtained by Formaggia et al. [21]. Both estimates in fact show that $E^{n+1} + \Delta t \sum_{i=1}^{n+1} G^i$ is bounded by the initial and boundary data as well as by a small constant arising from smooth mesh movement.

Remark 3.2 (Energy estimate for the midpoint rule.) *In what follows we will apply the midpoint rule in order to approximate convective term in the ALE formulation and show that we can derive corresponding energy estimate of the semi-discrete scheme without any dependence on the domain velocity \mathbf{w} , i.e. α^i, β^i from (61). Applying the midpoint rule for the ALE convective term the semi-discrete scheme reads*

$$\begin{aligned}
& \int_{\Omega^n} \tilde{\mathbf{u}}^{n+1} \cdot \frac{\tilde{\mathbf{u}}^{n+1} - \mathbf{u}^n}{\Delta t} \, d\omega + \frac{2}{\rho_f} \int_{\Omega^n} \mu(|\mathbf{D}(\tilde{\mathbf{u}}^{n+1})|) \mathbf{D}(\tilde{\mathbf{u}}^{n+1}) : \mathbf{D}(\tilde{\mathbf{u}}^{n+1}) \, d\omega \\
& + \frac{1}{2} \int_{\Omega^{n+1/2}} |\hat{\mathbf{u}}^{n+1}|^2 \nabla \cdot \mathbf{w}^{n+1/2} \, d\omega = -\frac{\rho_s h}{\rho_f} \int_{\Gamma_{wall}^0} \left[\frac{\xi^{n+\frac{1}{2}} - \xi^n}{\Delta t} \right] \xi^{n+\frac{1}{2}} \, dl_0 \\
& - \frac{\rho_s h c}{\rho_f} \int_{\Gamma_{wall}^0} \left[\frac{\partial \xi^{n+\frac{1}{2}}}{\partial x_1} \right]^2 \, dl_0 + \frac{1}{\rho_f} \int_{\Omega^n} \tilde{\mathbf{u}}^{n+1} \cdot \mathbf{f}^{n+1} \, d\omega - \frac{1}{\rho_f} \int_{\Gamma_{wall}^n} \frac{P_{ext}(t^{n+1}) \tilde{u}_2^{n+1}}{\sqrt{1 + (\partial_{x_1} R_0)^2}} \, dl \\
& + \frac{1}{\rho_f} \int_0^{R_0(0)} P_{in}(t^{n+1}) \tilde{u}_1^{n+1}|_{x_1=0} \, dx_2 - \frac{1}{\rho_f} \int_0^{R_0(L)} P_{out}(t^{n+1}) \tilde{u}_1^{n+1}|_{x_1=L} \, dx_2, \tag{63}
\end{aligned}$$

where $\hat{\mathbf{u}}^{n+1} = \mathbf{u}^{n+1} \circ A_{t^{n+1}} \circ A_{t^{n+1/2}}^{-1}$ is defined on $\Omega^{n+1/2}$. Analogously as before, using the estimates (31), (33), (35)-(41) and (44) we obtain

$$\begin{aligned}
& \|\tilde{\mathbf{u}}^{n+1}\|_{L^2(\Omega^n)}^2 + \Delta t \int_{\Omega^{n+1/2}} |\hat{\mathbf{u}}^{n+1}|^2 \nabla \cdot \mathbf{w}^{n+1/2} \, d\omega + C^* \Delta t \|\tilde{\mathbf{u}}^{n+1}\|_{W^{1,q}(\Omega^n)}^q \\
& + \frac{\rho_s h}{\rho_f} \left[\|\xi^{n+\frac{1}{2}}\|_{L^2(\Gamma_{wall}^0)}^2 - \|\xi^n\|_{L^2(\Gamma_{wall}^0)}^2 + 2\Delta t c \|\xi_{x_1}^{n+\frac{1}{2}}\|_{L^2(\Gamma_{wall}^0)}^2 \right] \\
& \leq \|\mathbf{u}^n\|_{L^2(\Omega^n)}^2 + \frac{2\Delta t C_2}{\varepsilon^{q'/q}} \text{RHS}^{n+1} + 2C^* \kappa \Delta t, \tag{64}
\end{aligned}$$

where RHS^{n+1} is defined in (43). Now, let us use the midpoint rule for time integration of the right hand side of the geometric conservation law condition (47), i.e.

$$\int_{t^n}^{t^{n+1}} \int_{\Omega_t} |\tilde{\mathbf{u}}|^2 \nabla \cdot \mathbf{w} \, d\omega \, dt = \Delta t \int_{\Omega^{n+1/2}} |\hat{\mathbf{u}}^{n+1}|^2 \nabla \cdot \mathbf{w}^{n+1/2} \, d\omega. \tag{65}$$

The main reason for this numerical integration arises from the analysis of flow problem with moving boundaries, where in two-dimensional case the integrand on the left hand side of (65) can be exactly computed using the midpoint integration rule, cf. [34, 39]. For three-dimensional domains exact integration of the double integral on the left hand side of (65) can be done using a special two-points quadrature rule as suggested in [34]. Moreover, we see that (65) balances out the term arising from the ALE derivative and we obtain the following estimate for the operator A

$$\begin{aligned}
& \|\mathbf{u}^{n+1}\|_{L^2(\Omega^{n+1})}^2 + C^* \Delta t \sum_{i=0}^n \|\tilde{\mathbf{u}}^{i+1}\|_{W^{1,q}(\Omega^i)}^q \\
& + \frac{\rho_s h}{\rho_f} \sum_{i=0}^n \left[\|\xi^{i+\frac{1}{2}}\|_{L^2(\Gamma_{wall}^0)}^2 - \|\xi^i\|_{L^2(\Gamma_{wall}^0)}^2 + 2\Delta t c \|\xi_{x_1}^{i+\frac{1}{2}}\|_{L^2(\Gamma_{wall}^0)}^2 \right] \\
& \leq \|\mathbf{u}^0\|_{L^2(\Omega_{ref})}^2 + \frac{2\Delta t C_2}{\varepsilon^{q'/q}} \sum_{i=1}^{n+1} \text{RHS}^i + 2C^* \kappa T. \tag{66}
\end{aligned}$$

Analogously as before, the final energy estimate is obtained by summing the contributions from the operator

A, cf. (66), and the operator B, cf. (60), i.e.

$$\begin{aligned}
& \|\mathbf{u}^{n+1}\|_{L^2(\Omega^{n+1})}^2 + \frac{\rho_s h}{\rho_f} \left[a \|\eta^{n+1}\|_{L^2(\Gamma_{wall}^0)}^2 + \frac{b}{2} \|\eta^{n+1}\|_{L^2(\Gamma_{wall}^0)}^2 + \|\xi^{n+1}\|_{L^2(\Gamma_{wall}^0)}^2 \right] \\
& + C^* \Delta t \sum_{i=0}^n \|\tilde{\mathbf{u}}^{i+1}\|_{W^{1,q}(\Omega^i)}^q + \frac{2\rho_s h c}{\rho_f} \Delta t \sum_{i=0}^n \|\xi_{x_1}^{i+\frac{1}{2}}\|_{L^2(\Gamma_{wall}^0)}^2 \\
& \leq \|\mathbf{u}^0\|_{L^2(\Omega_{ref})}^2 + \frac{\rho_s h}{\rho_f} \left[a \|\eta_{x_1}^0\|_{L^2(\Gamma_{wall}^0)}^2 + \frac{3b}{2} \|\eta^0\|_{L^2(\Gamma_{wall}^0)}^2 + \|\xi^0\|_{L^2(\Gamma_{wall}^0)}^2 \right] \\
& + \frac{2\Delta t C_2}{\varepsilon^{q'/q}} \sum_{i=1}^{n+1} \text{RHS}^i + \frac{\rho_s h a}{\rho_f} \frac{L|\Gamma_{wall}^0|}{\delta} + 2C^* \kappa T.
\end{aligned}$$

Thus, the total energy at the new time step t^{n+1} is bounded with the initial energy and the boundary data.

4 NUMERICAL MODELLING

The aim of this part is to analyse the second order kinematic splitting method numerically and illustrate its behaviour on a series of numerical experiments. In Section 4.1 we present our discretization methods used for the approximation of the fluid and structure. In Sections 4.2 and 4.3 numerical experiments illustrating behaviour of the kinematic splitting algorithm for a stenotic vessel and bifurcation geometry are presented. Section 4.4. is devoted to the numerical convergence study in space and time. Several important hemodynamic wall parameters for different constitutive models and different geometries are shown and discussed in Section 4.5. Finally in Section 4.6 an application of the kinematic splitting algorithm for three-dimensional fluid-structure interaction problem is presented.

4.1 DISCRETIZATION METHODS

Numerical scheme for fluid equations (5) is based on the finite volume method with use of the artificial compressibility stabilization, cf. [41, 42] UG-toolbox. The implicit Euler method, the Crank-Nicolson method or the second order backward differentiation formula can be applied for time discretization. For simplicity we present in what follows numerical scheme using the implicit Euler method. The nonlinear problem is solved via the Newton method. Structure equation (6) is discretized using the splitting approach (23)-(24) in time and finite differences in space. The operator A, cf. (28), is discretized as follows, see also [41, 42, 46] for more details,

$$\begin{aligned}
& \int_{\Omega_k^n} \begin{pmatrix} (\tilde{\mathbf{u}}_{\ell+1}^{n+1} - \mathbf{u}^n) \\ 0 \end{pmatrix} d\omega + \Delta t \int_{\Omega_k^n} \begin{pmatrix} (\nabla \cdot \mathbf{w}^n) \tilde{\mathbf{u}}_{\ell+1}^{n+1} \\ 0 \end{pmatrix} d\omega \\
& + \Delta t \int_{\partial\Omega_k^n} \begin{pmatrix} [(\tilde{\mathbf{u}}_{\ell}^{n+1} - \mathbf{w}^n) \cdot \mathbf{n}] \tilde{\mathbf{u}}_{\ell+1}^{n+1} + [(\tilde{\mathbf{u}}_{\ell+1}^{n+1} - \tilde{\mathbf{u}}_{\ell}^{n+1}) \cdot \mathbf{n}] \tilde{\mathbf{u}}_{\ell}^{n+1} \\ 0 \end{pmatrix} dl \\
& + \Delta t \int_{\partial\Omega_k^n} \begin{pmatrix} -(1/\rho_f) \mu(|\mathbf{D}(\tilde{\mathbf{u}}_{\ell}^{n+1})|) (\nabla \tilde{\mathbf{u}}_{\ell+1}^{n+1} \cdot \mathbf{n}) + (1/\rho_f) \tilde{p}_{\ell+1}^{n+1} (\mathbf{I} \cdot \mathbf{n}) \\ \tilde{\mathbf{u}}_{\ell+1}^{n+1} \cdot \mathbf{n} - (\Delta h)^2 \nabla (\tilde{p}_{\ell+1}^{n+1} - \tilde{p}_{\ell}^{n+1}) \cdot \mathbf{n} \end{pmatrix} dl = 0, \tag{67}
\end{aligned}$$

$$\frac{\xi^{n+1/2} - \xi^n}{\Delta t} = c\alpha \xi_{x_1 x_1}^{n+1/2} + c(1-\alpha) \xi_{x_1 x_1}^n + H(\tilde{p}_{\ell+1}^{n+1}, \tilde{\mathbf{u}}_{\ell+1}^{n+1}), \quad \alpha \in \{0.5; 1\}. \tag{68}$$

Here k is the index of control volume, n denotes time step, ℓ is the index of iteration in the Newton method and Δh denotes the grid size. For simplicity we assumed $\mathbf{f} = 0$. The Newmark scheme parameter α is chosen to be either 0.5 or 1. A new solution obtained from (67), (68) is the velocity $\tilde{\mathbf{u}}^{n+1}$ and the pressure \tilde{p}^{n+1} on Ω^n as well as the wall velocity function $\xi^{n+1/2}$ on Γ_{wall}^n .

Space discretization of each term in (67) follows the classical finite volume strategy, see [42, 46]. Considering a fixed time instant $t = t^{n+1}$ from $(0, T]$ a discrete computational domain Ω_h is assumed

to be covered by a polygonal dual mesh. The dual mesh consists of control volumes Ω_k , see Fig. 4, corresponding to the nodes (also called grid points) of the primary discretization of Ω_h . Note that it holds

$$\bar{\Omega}_h = \bigcup_{i=1}^{n_{gp}} \Omega_k, \quad \Omega_k \cap \Omega_j = \begin{cases} \text{boundary or empty set} & \text{if } k \neq j, \\ \Omega_k = \Omega_j & \text{if } k = j, \end{cases}$$

where n_{gp} denotes the number of grid points. Then for the control volume Ω_k corresponding to the grid point gp_k we denote by Ω_{kj} a subvolume of Ω_k , that has a common boundary with its neighbour Ω_j . In particular $j \in s(k)$, where $s(k)$ denotes the set of all neighbouring control volumes to Ω_k . Finally, in the middle of each straight segment of the subcontrol volume boundary Ω_{kj} we define the so-called integration point ip_{kj} , cf. Fig. 4.

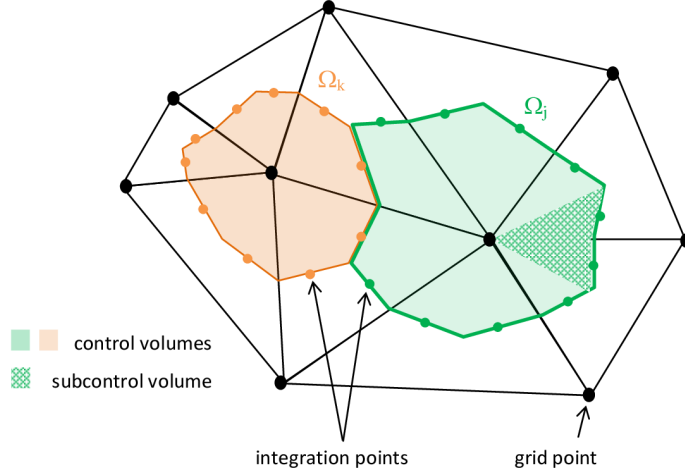


Figure 4: A possible grid arrangement for the finite volume method. Each control volume is represented by a grid point (gp) and a set of integration points (ip).

To illustrate space discretization of (67) let us describe the approximation of the convective and the viscous term. First, the approximation of the convective term is as follows

$$\begin{aligned} & \int_{\partial\Omega_k^n} \left(\tilde{\mathbf{u}}_{\ell+1}^{n+1} \left[(\tilde{\mathbf{u}}_{\ell}^{n+1} - \mathbf{w}^n) \cdot \mathbf{n}_k \right] + \tilde{\mathbf{u}}_{\ell}^{n+1} \left[(\tilde{\mathbf{u}}_{\ell+1}^{n+1} - \tilde{\mathbf{u}}_{\ell}^{n+1}) \cdot \mathbf{n}_k \right] \right) dl \\ & \approx \sum_{j \in s(k)} \left(\tilde{\mathbf{u}}_{\ell+1}^{up, n+1}(ip_{kj}) \left[N_k(ip_{kj}) \tilde{\mathbf{u}}_{\ell}^{n+1}(gp_k) \cdot \bar{\mathbf{n}}(ip_{kj}) - N_k(ip_{kj}) \mathbf{w}^n(gp_k) \cdot \bar{\mathbf{n}}(ip_{kj}) \right] \right. \\ & \quad \left. + N_k(ip_{kj}) \tilde{\mathbf{u}}_{\ell}^{n+1}(gp_k) \left[\tilde{\mathbf{u}}_{\ell+1}^{up, n+1}(ip_{kj}) \cdot \bar{\mathbf{n}}(ip_{kj}) - N_k(ip_{kj}) \tilde{\mathbf{u}}_{\ell}^{n+1}(gp_k) \cdot \bar{\mathbf{n}}(ip_{kj}) \right] \right), \end{aligned}$$

where $\bar{\mathbf{n}}(ip_{kj}) := \mathbf{n}(ip_{kj}) |\partial\Omega_{kj}^n|$ denotes the outward normal vector corresponding to the integration point ip_{kj} , $|\partial\Omega_{kj}^n|$ represents the area of the subcontrol volume boundary $\partial\Omega_{kj}$ at the time instant $t = t^n$, N_k is the linear nodal basis and $\tilde{\mathbf{u}}_{\ell+1}^{up, n+1}(ip_{kj})$ is the upwind velocity at the integration point ip_{kj} . The viscous term is approximated in the following way

$$\begin{aligned} & \int_{\partial\Omega_k^n} \mu(|\mathbf{D}(\tilde{\mathbf{u}}_{\ell}^{n+1})|) \nabla \tilde{\mathbf{u}}_{\ell+1}^{n+1} \cdot \mathbf{n}_k dl \approx \sum_{j \in s(k)} \int_{\partial\Omega_{kj}^n} \mu(|\mathbf{D}(\tilde{\mathbf{u}}_{\ell}^{n+1})|) \nabla \tilde{\mathbf{u}}_{\ell+1}^{n+1} \cdot \mathbf{n}_{kj} dl \\ & \approx \sum_{j \in s(k)} \mu \left(\left| \mathbf{D}(N_k(ip_{kj}) \tilde{\mathbf{u}}_{\ell}^{n+1}(gp_k)) \right| \right) \nabla N_k(ip_{kj}) \tilde{\mathbf{u}}_{\ell+1}^{n+1}(gp_k) \cdot \bar{\mathbf{n}}(ip_{kj}). \end{aligned}$$

Let us note that in order to impose boundary condition (13) we just need to set the sum of the corresponding boundary integrals along $\partial\Omega_{kj}^n \subset \Gamma_{out}$ arising from the convective and viscous terms to $\int_{\partial\Omega_{kj}^n} P_{out} \mathbf{n}_{kj} dl$; inflow boundary condition (12) can be imposed in an analogous way.

In the second step of the operator splitting approach the operator B is approximated. It combines the purely elastic part of structure equation and the kinematic splitting condition. The latter defines time derivative of the wall displacement η , which is the velocity ξ . An explicit scheme reads as follows

$$\begin{aligned} \frac{\eta^{n+1} - \eta^n}{\Delta t} &= \alpha_1 \xi^{n+1/2} + (1 - \alpha_1) \xi^n, \\ \frac{\xi^{n+1} - \xi^{n+1/2}}{\Delta t} &= a\alpha_2 \eta_{x_1 x_1}^{n+1} + a(1 - \alpha_2) \eta_{x_1 x_1}^n - b\alpha_2 \eta^{n+1} - b(1 - \alpha_2) \eta^n + G(R_0) \end{aligned} \quad (69)$$

for $\alpha_1 = 0.5$, $\alpha_2 \in \{0.5; 1\}$. An implicit scheme has the following form

$$\begin{aligned} \frac{\eta^{n+1} - \eta^n}{\Delta t} &= \alpha_1 \xi^{n+1} + (1 - \alpha_1) \xi^{n+1/2}, \\ \frac{\xi^{n+1} - \xi^{n+1/2}}{\Delta t} &= a\alpha_2 \eta_{x_1 x_1}^{n+1} + a(1 - \alpha_2) \eta_{x_1 x_1}^n - b\alpha_2 \eta^{n+1} - b(1 - \alpha_2) \eta^n + G(R_0) \end{aligned} \quad (70)$$

for $\alpha_1 = 0.5$, $\alpha_2 = 0.5$. Note that $\xi^{n+1/2}$ used in (69)-(70) is obtained in (68). In our experiments we have used both the explicit as well as the implicit method, cf. (69)-(70). The implicit coupling was typically more stable. We note that once new values for the wall displacement η^{n+1} and the velocity ξ^{n+1} are known, we update the fluid velocity on the moving boundary to \mathbf{u}^{n+1} as well as the geometry. Let us point out that the operator $H(\mathbf{u}, p)$, cf. (8), has a term $R/R_0 = (R_0 + \eta)/R_0$. For technical reasons in our numerical experiments we insert a part having the factor η/R_0 in the operator B. As a consequence b -term in the code has the following form

$$\tilde{b} := b + \frac{(P_{ext} \mathbf{I} + \mathbf{T}) \mathbf{n} \cdot \mathbf{e}_r}{\rho_s h R_0} \frac{\sqrt{1 + (\partial_{x_1} R)^2}}{\sqrt{1 + (\partial_{x_1} R_0)^2}}.$$

This is motivated by the fact that we want to separate η from the equation (23)₃, which results in a parabolic equation only for ξ .

Remark 4.1 (On time discretization by the operator splitting scheme) *Fluid-structure interaction problem (68)-(69) or (68)-(70) can be rewritten in the following way*

$$\mathcal{U}^{n+1} = B_{\Delta t} A_{\Delta t} \mathcal{U}^n, \quad (71)$$

where \mathcal{U}^n is the approximate solution of coupled problem at the time level t^n and $A_{\Delta t}$ and $B_{\Delta t}$ denote the operator A, cf. (23), and the operator B, cf. (24), acting on interval $(t^n, t^{n+1}]$, $\Delta t = t^{n+1} - t^n$, respectively. The scheme (71) is known as the Marchuk-Yanenko splitting scheme, which is of the first order. The accuracy of our time-splitting scheme can be improved using the second order Strang splitting scheme, i.e.

$$\mathcal{U}^{n+1} = B_{\Delta t/2} A_{\Delta t} B_{\Delta t/2} \mathcal{U}^n. \quad (72)$$

Here $B_{\Delta t/2}$ denotes the operator B acting on the interval of length $\Delta t/2$. Both schemes (71)-(72) belong to the class of operator splitting methods commonly used for time discretization of initial valued problems, see [26] for more detail. In our numerical experiments, see Section 4.4, both time-splitting schemes have been used successfully and (72) increases the convergence rate in time.

4.2 COMPUTATIONAL GEOMETRY AND PARAMETER SETTING

Numerical experiments have been done for different reference geometries with both constant as well as non-constant reference radius R_0 . The geometry shown in Fig. 3 is used for analysis of the experimental

order of convergence. Here we set $R_0 = 1$ cm. Fig. 5 illustrates a stenotic vessel and Fig. 6 represents a bifurcation geometry. In the case of stenotic reference geometry, the reference radius is prescribed in the following way

$$R_0(x_1) = \begin{cases} R_0(0) \left[1 - 0.15 \left(1 + \cos \left(\frac{5 \pi (x_1 - L/2)}{L} \right) \right) \right] & \text{if } x_1 \in [0.3L; 0.7L], \\ R_0(0) & \text{if } x_1 \in [0; 0.3L) \cup (0.7L; L], \end{cases} \quad (73)$$

where L denotes the length of vessel. In the experiments with prescribed sinus pulses on the inflow boundary, we set $R_0(0) = 1$ cm and $L = 10$ cm. Taking into account physiological pulses prescribed by the iliac flow rate (Fig. 7, left), the radius $R_0(0) = 0.6$ cm and the length $L = 6$ cm were chosen. This radius represents the physiological radius of an iliac artery, i.e. a daughter artery of the abdominal aorta bifurcation, cf. [51].

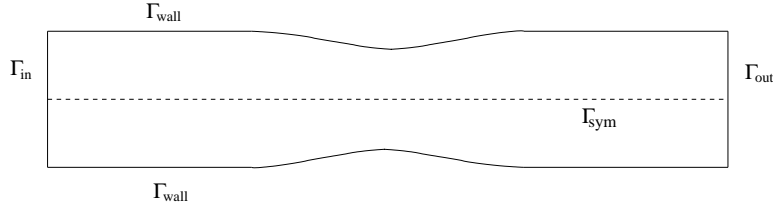


Figure 5: Stenotic reference geometry.

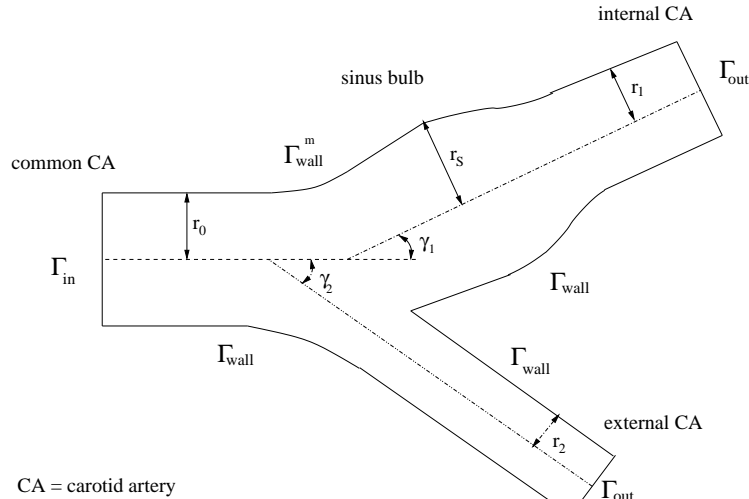


Figure 6: Bifurcation reference geometry, see [44].

The bifurcation geometry shown in Fig. 6 represents a more complex geometry with asymmetric daughter vessels and the so-called sinus bulb area. It is a simplified example of a realistic carotid artery bifurcation, see [44]. The radii of the mother vessel (i.e. common carotid artery), daughter vessels (i.e. external and internal carotid artery) and the maximal radius of the sinus bulb area are: $r_0 = 0.31$ cm, $r_1 = 0.22$ cm, $r_2 = 0.18$ cm and $r_S = 0.33$ cm. The branching angles for the bifurcation in Fig. 6 are $\gamma_1 = \gamma_2 = 25^\circ$.

We note that since the generalized string model has been derived for radially symmetric domains we need to preserve the radial symmetry for each single vessel of the carotid bifurcation. For this purpose we need to follow the axis of symmetry in order to compute the wall deformation η . In the situation depicted in Fig. 6 it would mean to rotate the original coordinate system with respect to the bifurcation angle γ_1 (for the internal carotid artery) and the bifurcation angle γ_2 (for the external carotid artery). In our simulations for simplicity we assume that only one part of boundary Γ_{wall} (this corresponds to the boundary Γ_{wall}^m in Fig. 6) is allowed to move. Although our two-dimensional mathematical model is

simplified the choice of upper boundary has a physiological motivation. It is well-known that atherosclerosis occurs preferably at the outer wall of daughter vessel, especially in the carotid sinus, see [35]. Therefore this area is of special interest. Note that we use two different reference frames. The first one corresponds to the mother vessel and in the second one the x_1 -axis coincides with the axis of symmetry of the internal daughter vessel. To be more precise, it means that we introduce a new coordinate system $(\bar{x}_1, \bar{x}_2) \in \mathbb{R}^2$, i.e.

$$\bar{x}_1 = (x_1 - 0.9) \cos \gamma_1 + (x_2 + 0.05) \sin \gamma_1, \quad (74)$$

$$\bar{x}_2 = (0.9 - x_1) \sin \gamma_1 + (x_2 + 0.05) \cos \gamma_1. \quad (75)$$

Note that also the fluid load in the dynamic coupling condition (6), represented by the Cauchy stress applied to the walls, will be transformed into the coordinate system (74) - (75).

In what follows a parabolic inflow profile is prescribed on the inflow boundary, i.e.

$$\mathbf{u}_{in}((0, x_2), t) = \frac{R(0, t)^2 - x_2^2}{R(0, t)^2} f(t) \mathbf{e}_r,$$

where $R(0, t) = R_0(0) + \eta(0, t)$ and $f(t)$ denotes a temporal function. In our experiments we have used a function that describes sinus pulses of heart, i.e

$$f(t) = U_0 \sin^2(\pi t/\omega), \quad t \in I \quad \text{with} \quad \omega = 1 \text{ s} \quad \text{or} \quad \omega = 0.9 \text{ s}, \quad (76)$$

where U_0 is the maximal inflow u_1 -velocity and ω represents the period of one heart beat. Moreover, considering physiological pulses of heart, the temporal function depending on the flow rate $Q(t)$ in artery was prescribed, see Fig. 7. From the definition of the flow rate $Q(t) = \int_{\Gamma_{in}} u_{in,1} dS$ we obtain

$$f(t) = \frac{2Q(t)}{\pi R(0, t)^2}, \quad t \in I. \quad (77)$$

Here we note that the mean inflow velocity and the maximal inflow velocity are defined by

$$\bar{U} = \frac{Q(t)}{\pi R(0, t)^2}, \quad U_0 = \frac{2Q(t)}{\pi R(0, t)^2},$$

respectively. For outflow boundary condition (13) we set $P_{out} = 0$.

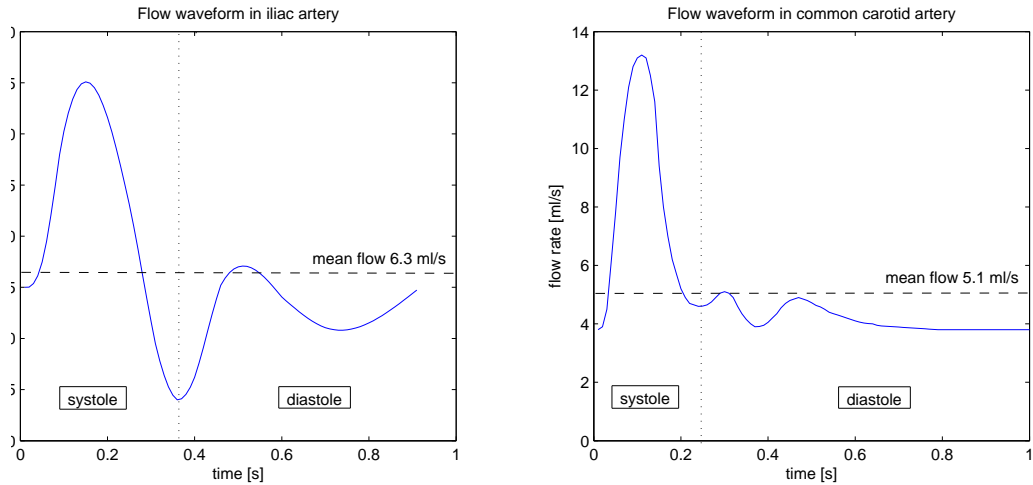


Figure 7: Flow rate $Q(t)$ in iliac artery (left) and in common carotid artery (right), see [44, 51].

In the Tab. 1 the fluid and the structure model parameters are specified. Suitable parameters for the non-Newtonian viscosity models (2) and (3) are prescribed in the Tab. 2, see also [55].

Table 1: Fluid and structure model parameters.

Fluid parameters			
Newt. viscosity (in physiol. exp.)	μ	0.0345	P
Newt. viscosity (in model exp.)	μ	0.63	P
fluid density	ρ_f	1	g.cm^{-3}
Structure parameters			
wall density	ρ_s	1.1	g.cm^{-3}
wall thickness	h	0.1	cm
Young's modulus	E	0.75×10^5	dyn.cm^{-2}
Poisson's ratio	$\tilde{\xi}$	0.5	[1]
Timoshenko's factor	κ	1	[1]
viscoelasticity constant	γ	2×10^4	P.s.cm^{-1}

Table 2: Non-Newtonian model parameters.

Carreau model		Yeleswarapu model	
model data	physiological data	model data	physiological data
$\mu_0 = 1.26 \text{ P}$	$\mu_0 = 0.56 \text{ P}$	$\mu_0 = 1.26 \text{ P}$	$\mu_0 = 0.736 \text{ P}$
$\mu_\infty = 0.63 \text{ P}$	$\mu_\infty = 0.0345 \text{ P}$	$\mu_\infty = 0.63 \text{ P}$	$\mu_\infty = 0.05 \text{ P}$
$p = 1.6$	$p = 1.356$	$\Lambda = 14.81$	$\Lambda = 14.81$
$\lambda = 1$	$\lambda = 3.313$	$U_0 = 38 \text{ cm.s}^{-1}$	
$U_0 = 38 \text{ cm.s}^{-1}$			

In Section 4.4 the model data for the Newtonian and the non-Newtonian viscosity function from Tab. 2 were used for the analysis of the experimental order of convergence. For the inflow boundary data we have used the Dirichlet boundary condition with a prescribed parabolic velocity constant in time, the maximum U_0 is given in Table 2. Consequently, the Reynolds number is $\text{Re} \in [30; 60]$. On the other hand the hemodynamic wall parameters, presented in Section 4.5, were computed for stenotic as well as bifurcation geometry using the physiological parameters from Tab. 2 and the inflow data specified in (77), cf. also Figure 7.

In the human circulatory system, the Reynolds number varies quite significantly. Over one cycle it reaches the values from 10^{-3} up to 6000. A typical critical number for a normal artery is around 2300, for bifurcation it is around 600. However, the recirculation zones start to be created already at the Reynolds number around 170. This explains the fact that small recirculation zones appear even in healthy bifurcations. The part of a bifurcation that is the most sensitive to the local change of flow is the so-called sinus bulb area. This is a part of a daughter vessel, where an atherosclerosis is usually formed, see Fig. 6. Indeed, our analysis of the local hemodynamic parameters (Section 4.5) confirms this fact.

In the following we give the overview of the Reynolds numbers Re_0 and Re_∞ defined by

$$\text{Re}_0 := \frac{\rho_f |\bar{U}| 2R_0(0)}{\mu_0}, \quad \text{Re}_\infty := \frac{\rho_f |\bar{U}| 2R_0(0)}{\mu_\infty}, \quad (78)$$

respectively, for the experiments presented in the next sections. Note that in the Newtonian case we have $\text{Re} = \text{Re}_\infty$. In the Tab. 3 and Tab. 4 the Reynolds numbers for the experiments with physiological pulses corresponding to the carotid artery flow rate (Fig. 7, right) and the iliac artery flow rate (Fig. 7, left), respectively, are computed. We denote by Q_{mean} , Q_{max} and Q_{min} the mean, the maximal and the minimal flow rate, respectively. We can observe that in the case of carotid artery the Reynolds numbers corresponding to the mean flow are higher than the ones corresponding to the iliac artery. Consequently, larger recirculation zones can appear in the iliac arteries. We note here that the Newtonian viscosity corresponds to μ_∞ in the Carreau model and therefore the Reynolds numbers for these two cases coincide.

Table 3: Reynolds numbers for physiological data and physiological pulses for the common carotid artery.

	Newtonian model	Carreau model	Yeleswarapu model
	$R_0(0) = 0.31$ cm	$R_0(0) = 0.31$ cm	$R_0(0) = 0.31$ cm
$Q_{mean} = 5.1$ ml.s ⁻¹ $\bar{U} = 16.9$ cm.s ⁻¹	Re \approx 304	Re ₀ \approx 19 Re _∞ \approx 304	Re ₀ \approx 14 Re _∞ \approx 210
$Q_{max} = 13.2$ ml.s ⁻¹ $\bar{U} = 43.7$ cm.s ⁻¹	Re \approx 785	Re ₀ \approx 48 Re _∞ \approx 785	Re ₀ \approx 37 Re _∞ \approx 542
$Q_{min} = 3.9$ ml.s ⁻¹ $\bar{U} = 12.9$ cm.s ⁻¹	Re \approx 232	Re ₀ \approx 14 Re _∞ \approx 232	Re ₀ \approx 11 Re _∞ \approx 160

Table 4: Reynolds numbers for physiological data and physiological pulses for the iliac artery.

	Newtonian model	Carreau model	Yeleswarapu model
	$R_0(0) = 0.6$ cm	$R_0(0) = 0.6$ cm	$R_0(0) = 0.6$ cm
$Q_{mean} = 6.3$ ml.s ⁻¹ $\bar{U} = 5.6$ cm.s ⁻¹	Re \approx 195	Re ₀ \approx 12 Re _∞ \approx 195	Re ₀ \approx 9 Re _∞ \approx 134
$Q_{max} = 25.1$ ml.s ⁻¹ $\bar{U} = 22.2$ cm.s ⁻¹	Re \approx 772	Re ₀ \approx 48 Re _∞ \approx 772	Re ₀ \approx 36 Re _∞ \approx 533
$Q_{min} = -6.0$ ml.s ⁻¹ $\bar{U} = -5.3$ cm.s ⁻¹	Re \approx 185	Re ₀ \approx 14 Re _∞ \approx 185	Re ₀ \approx 10 Re _∞ \approx 114

4.3 EXPERIMENTS

In our numerical experiments the computational domain Ω_{ref} is covered by a mesh consisting of quadrilateral finite volumes. Each mesh element is characterized by a space step $\Delta h := \min\{\Delta x_1, \Delta x_2\}$, where Δx_1 and Δx_2 denotes the space step in x_1 -direction and x_2 -direction, respectively. Considering the bifurcation geometry the domain was discretized into 3072 elements and in the case of stenotic geometry 2048 elements built the grid. The corresponding time step for simulations was $\Delta t = 0.001$ s (stenotic geometry) and $\Delta t = 0.0005$ s (bifurcation geometry). Let us point out that before starting to compute the fluid-structure interaction problem (68)-(70) with moving boundaries a precomputation for a corresponding rigid domain has been done. This preprocessing takes one period of heart beat.

In what follows we present the results of numerical experiments using the kinematic coupling fluid-structure interaction algorithm (68)-(70). In Fig. 8 streamlines and velocity vector field for bifurcation geometry are displayed. The plot in Fig. 8a corresponds to the systolic peak flow. Pressures and velocities are from the range $[-46.4, 291]$ Pa and $[0, 87.7]$ cm.s⁻¹, respectively. In the systolic deceleration phase, see Fig. 8b, reversed flow appears. This can be visibly seen in the daughter vessels, especially in the carotid sinus bulb. Recirculation zones are also visible in the plots of streamlines. After reaching the diastolic maximum, see Fig. 8c, reversed flow in the sinus bulb further develops. Similarly as in the previous plot, the streamlines and velocities have changed due to the diastolic deceleration phase of the cycle. Now, pressure is from the interval $[-7.6, 28.2]$ Pa and the velocities belong to $[0, 26.9]$ cm.s⁻¹. Finally, in Fig. 8d, results for diastolic flow are displayed. The plot represents the situation at the end of one cardiac cycle. We can note that due to the bifurcation geometry the axial velocity profiles in daughter vessels are asymmetric.

In Fig. 9 we can see more precisely the evolution of the wall deformation function η in time along the moving boundary. The curves in Fig. 9 (left) correspond to the significant time instants of the physiological flow for common carotid artery. In particular, we have at $t = 0.1$ s the systolic maximum, at $t = 0.23$ s the systolic minimum, at $t = 0.36$ s the diastolic minimum and $t = 0.96$ s corresponds to the final phase of one heart beat. We observe that the deformation is larger in the area of sinus bulb. This is caused by decreasing stresses, which directly influence the wall deformation. We point out that considering several constitutive models for viscosity function only slight differences in the deformation appear, see

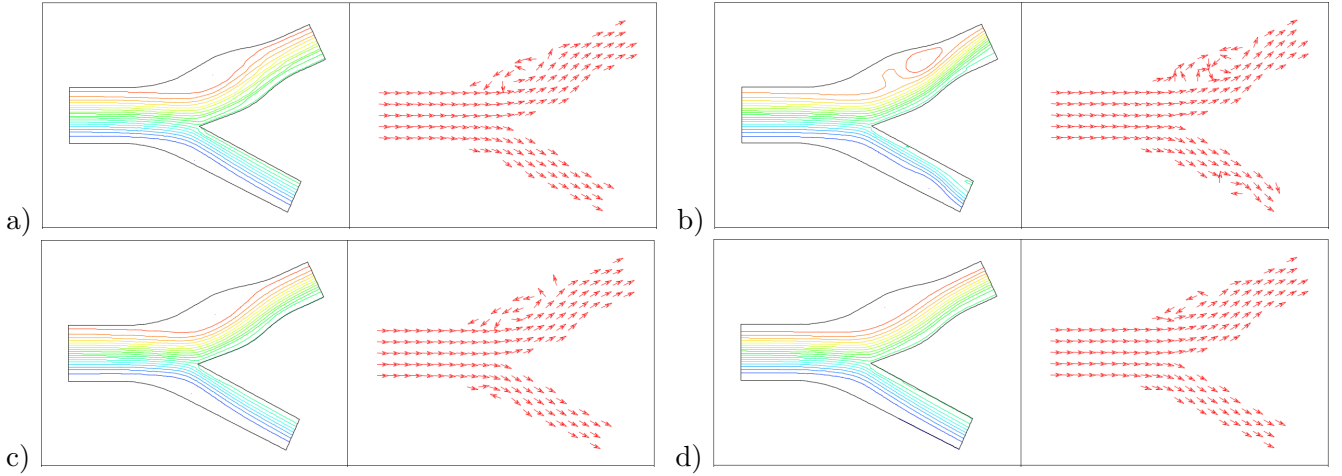


Figure 8: Streamlines and velocity vector field for bifurcation at four time instants: a) $t = 0.10s$, b) $t = 0.23s$, c) $t = 0.36s$, d) $t = 0.96s$. Carreau model with physiological data and physiological pulses.

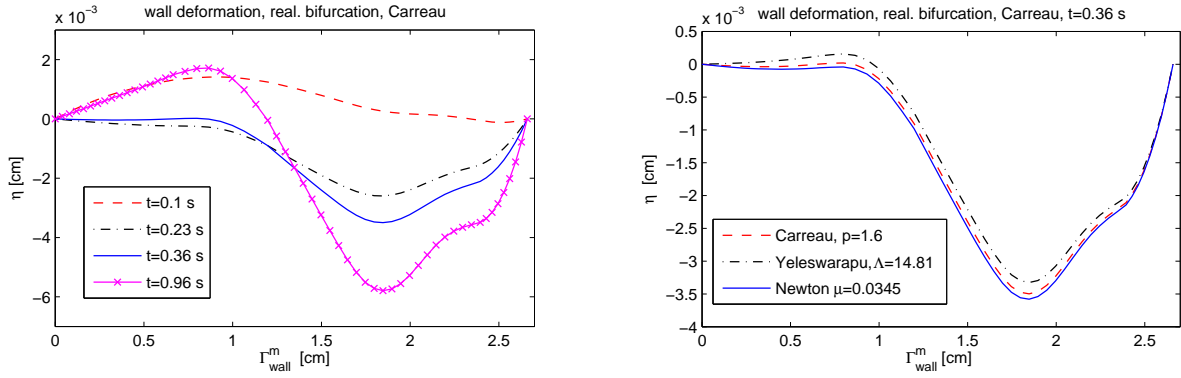


Figure 9: The evolution of η along the moving boundary Γ_{wall}^m for bifurcation geometry. Left: comparison at different time instants, right: comparison of constitutive models at $t = 0.36 s$.

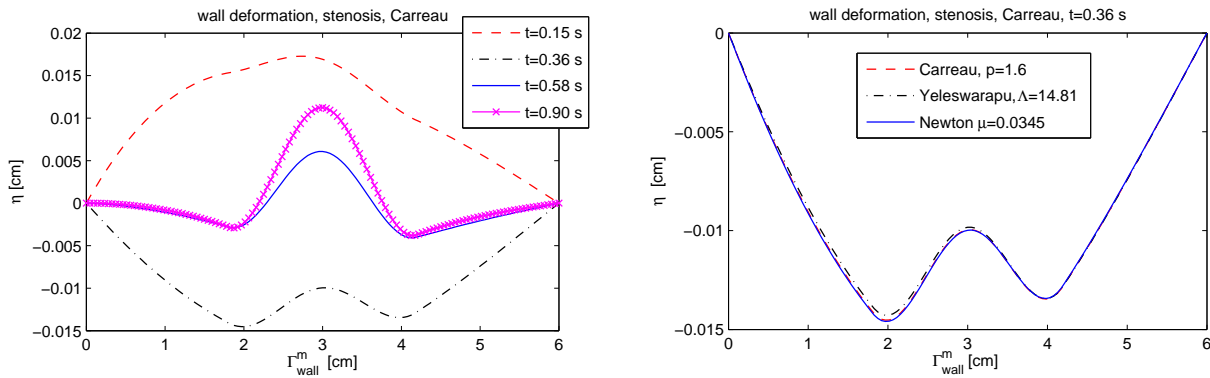


Figure 10: The evolution of η along the line $x_2 = R_0$ for stenosed vessel. Left: comparison at several time instants, right: comparison of constitutive models at $t = 0.36 s$.

Fig. 9 (right). Therefore we can conclude that the non-Newtonian rheology does not significantly influence the wall displacement.

In order to demonstrate the dependence of the wall movement on the reference geometry of vessel, we compare the results for bifurcation geometry from Fig. 9 with the ones for stenotic geometry plotted in Fig. 10. We see again that, as it is expected, the presence of a stenosed region has influence on the compliance of vessel wall.

In Fig. 12 results for the stenosed iliac artery are presented. In each subpart, from the top to the bottom, the streamlines, pressure isolines, velocity vector field and u_1 -velocity isolines are plotted. The time instant $t = 0.15$ s corresponds to the flow rate maximum, i.e. the systolic peak flow, with velocities and pressures from the range $[0, 45.4]$ cm.s^{-1} and $[-38.4, 26.2]$ Pa, respectively. Passing the systolic deceleration phase, a reversed flow develops (Fig. 12b) and spreads in almost the whole domain (Fig. 12c). Indeed, at $t = 0.27$ s we observe in the plot of streamlines and the velocity field isolines the recirculation zones after and before the stenosed part of vessel. At the systolic minimum $t = 0.36$ s the negative flow with pressures from $[-51.6, 0]$ Pa and u_1 -velocities from $[-21.5, 7.8]$ cm.s^{-1} develops. This is furthermore visible in the early diastolic phase. Finally, passing through the diastolic maximum a secondary reversed flow appears. As it is expected, it starts to develop around the stenosed parts. This can be observed in Fig. 12d).

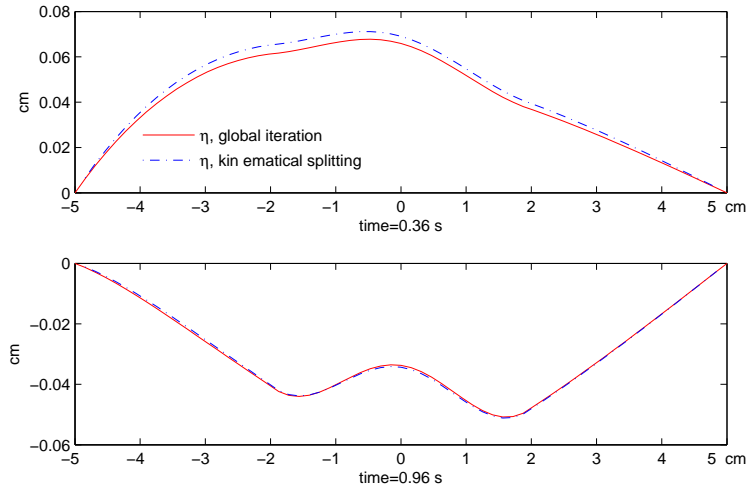


Figure 11: Comparison of the wall deformation η in stenosed vessel for the global iterative method and the explicit kinematic splitting; Carreau model: $\mu_0 = 1.26$ P, $\mu_\infty = 2.53$ P, $\lambda = 1$, $q = 1.356$.

Finally, in Fig. 11, let us compare our new kinematic splitting scheme with the so-called global iterative method developed by Hundertmark and Lukáčová [30]. The global iterative method is a strong coupling method based on the decoupling of fluid-structure interaction using global iterations with respect to the domain geometry. More precisely, we first fix a computational domain $\Omega(\eta^{(k-1)})$ for some given $\eta^{(k-1)}$, k is an iteration index, and compute numerically both fluid as well as structure equations for the whole time interval I . Afterwards we compare new and old iterations of η ; $\eta^{(k)} - \eta^{(k-1)}$. In order to obtain that the consequent global iterations of η differ by less than 10^{-5} approximately 5 to 6 global iterations are typically needed.

Clearly, the kinematic scheme is affected by the splitting error whereas the solution of the global iterative scheme is not. Nevertheless our numerical error analysis indicates that both methods are comparable, cf. Tabs. 5 and 6 in Section 4.4. Moreover, our new loosely coupled kinematic scheme is more efficient since it does not require additional iterations as it is the case of the global iterative scheme. Our extensive numerical experiments show that the kinematic coupling scheme needs approximately 5 times less CPU than the global iterative scheme.

4.4 CONVERGENCE STUDY

In order to study the accuracy of the coupled fluid-structure interaction problem the so-called *experimental order of convergence* (EOC) in space and time is computed.

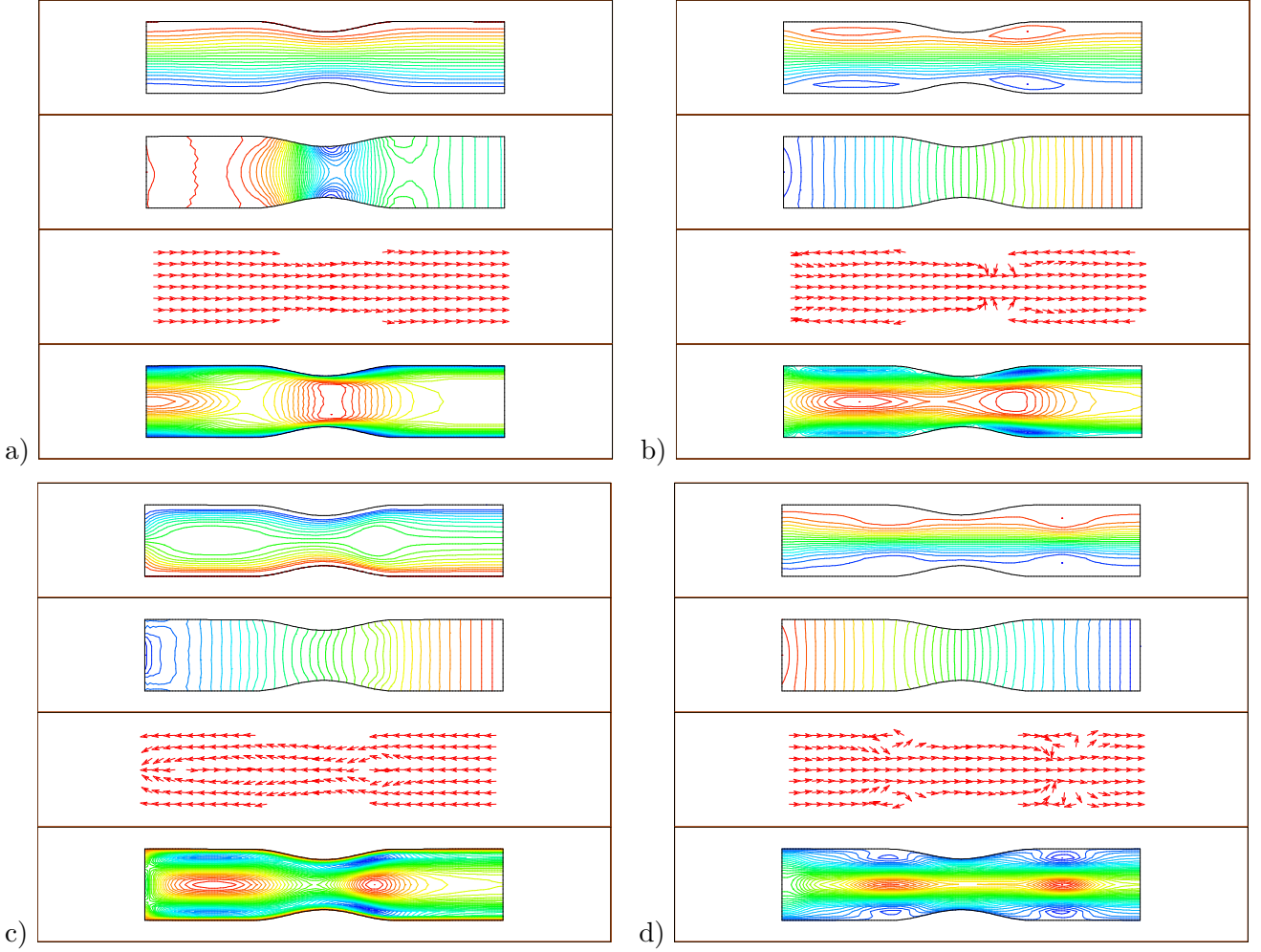


Figure 12: Streamlines, pressure isolines, velocity vector field and u_1 -velocity isolines for stenosed vessel at four different time instants: a) $t = 0.15\text{s}$, b) $t = 0.27\text{s}$, c) $t = 0.36\text{s}$, d) $t = 0.8\text{s}$. Carreau model with physiological data and physiological pulses.

4.4.1 Experimental order of convergence in space

In the first experiment we compare results obtained from the kinematic splitting algorithm, see Tab. 6, with the global iterative scheme of Hundertmark and Lukáčová, cf. [30], see Tab. 5. In what follows we will present the convergence results in space in term of the EOC values for velocity, gradient of velocity, pressure and domain displacement. As in [30] the EOC in space is defined in the following way

$$EOC(\mathbf{u}) = \log_2 \frac{\|\mathbf{u}_{\Delta h, \Delta t} - \mathbf{u}_{\Delta h/2, \Delta t}\|_{L^q} / |\Omega_{\Delta h}|^{1/q}}{\|\mathbf{u}_{\Delta h/2, \Delta t} - \mathbf{u}_{\Delta h/4, \Delta t}\|_{L^q} / |\Omega_{\Delta h/2}|^{1/q}}, \quad (79)$$

where $|\Omega_{\Delta h}|$ denotes the area of $\Omega_{\Delta h}$. Moreover, let us define a normalized L^q error by

$$Err(\mathbf{u}) = \frac{\|\mathbf{u}_{\Delta h, \Delta t} - \mathbf{u}_{\Delta h/2, \Delta t}\|_{L^q}}{|\Omega_{\Delta h}|^{1/q}}. \quad (80)$$

Here $\mathbf{u}_{\Delta h, \Delta t}$ is the approximate velocity and $\Omega_{\Delta h}$ is the computational domain corresponding to the grid size Δh . Note that (79) and (80) are computed for a fixed space step Δt . The index q denotes a corresponding exponent in the power-law type model used for the non-Newtonian viscosity function (2). In our case the crucial value of q is 1.6. In the case of Newtonian flow L^2 norms (or H_0^1 norms) in space are used that corresponds to the space regularity of the weak solution, cf. [31], where the existence of weak solution of shear-dependent non-Newtonian fluids was analysed. The computational geometry used

in the experiments is shown in Fig. 3. Only the upper boundary Γ_{wall} is allowed to move. The grid was consecutively divided having 32, 128, 512, 2048 elements for different grid levels, the initial space step was $\Delta h = 0.625$ cm. Note that the EOC in space (79) was computed for the time instant $T = 0.8$ s. The fixed time step Δt was set to 0.002 s. We have used model data for the non-Newtonian Carreau viscosity function, see Tabs. 1, 2. We can clearly see the similar convergence rates in velocities, pressures and displacements. Note that our approach is more efficient, since it does not use additional iterations with respect to the domain as it is in the case for the strong coupling method (global iterative scheme), cf. [30]. Moreover, we see that the kinematic splitting yields 10 times smaller relative errors in the wall displacement than the strong coupling scheme.

Table 5: Convergence rates in space; strong coupling method, Carreau viscosity.

# refin (Δh)	$Err(\mathbf{u})$	$EOC(\mathbf{u})$	$Err(\eta)$	$EOC(\eta)$	$Err(p)$	$EOC(p)$
	L^q -norm			L^2 -norm		
2/1	0.9512		2.81 e-3		3.3925	
3/2	0.2563	1.89	8.88 e-4	1.69	0.7113	2.25
4/3	0.1074	1.26	1.85 e-4	2.23	0.1577	2.17

Table 6: Convergence rates in space; kinematic splitting scheme, Carreau viscosity.

# refin (Δh)	$Err(\mathbf{u})$	$EOC(\mathbf{u})$	$Err(\nabla\mathbf{u})$	$EOC(\nabla\mathbf{u})$	$Err(\eta)$	$EOC(\eta)$	$Err(p)$	$EOC(p)$
	L^q -norm				L^2 -norm			
2/1	0.8971		0.9682		2.62 e-4		3.1338	
3/2	0.2466	1.86	0.1408	2.78	1.84 e-5	0.51	0.7026	2.16
4/3	0.1051	1.23	0.0435	1.69	0.38 e-5	2.26	0.1461	2.27

In the second experiments we have computed a reference solution on the mesh having 32 768 elements and compared the L^2 or L^q norms of the difference between the reference \mathbf{u}_{ref} and the approximate solutions, respectively. Thus, the normalized L^q error is given as

$$Err(\mathbf{u}) = \frac{\|\mathbf{u}_{\Delta h, \Delta t} - \mathbf{u}_{ref}\|_{L^q}}{|\Omega_{\Delta h}|^{1/q}} \quad (81)$$

and the EOC is now computed in the following way

$$EOC(\mathbf{u}) = \log_2 \frac{\|\mathbf{u}_{\Delta h, \Delta t} - \mathbf{u}_{ref}\|_{L^q} / |\Omega_{\Delta h}|^{1/q}}{\|\mathbf{u}_{\Delta h/2, \Delta t} - \mathbf{u}_{ref}\|_{L^q} / |\Omega_{\Delta h/2}|^{1/q}}. \quad (82)$$

We have compared the convergence order in space for different variants of our kinematic splitting scheme. We present here the EOC results in space obtained by the explicit kinematic splitting scheme and the implicit Strang splitting approach; the explicit Strang splitting and implicit kinematic splitting scheme yield analogous results. As in the previous test, the different levels of grid refinements have 32, 128, 512 and 2048 elements, respectively. The final time was taken $T = 0.004$ s and a fixed time step $\Delta t = 10^{-4}$ s has been used.

We can see that both schemes have very similar error behaviour, in particular we get the second order convergence for velocities and pressures. As it is expected, the Strang splitting technique has not visibly influenced the convergence rates in space. We will see in the next subsection that the Strang splitting technique improves the experimental order of convergence in time.

Table 7: Convergence rates in space; explicit kinematic splitting scheme, Carreau viscosity.

# refin (Δh)	$Err(\mathbf{u})$	$EOC(\mathbf{u})$	$Err(\nabla\mathbf{u})$	$EOC(\nabla\mathbf{u})$	$Err(\eta)$	$EOC(\eta)$	$Err(p)$	$EOC(p)$
	L^q -norm				L^2 -norm			
1	0.24542		0.0219		0.2942		0.0695	
2	0.07939	1.63	0.0637	1.78	0.1087	1.44	0.0529	0.39
3	0.02861	1.46	0.0303	1.07	0.0425	1.35	0.0306	0.79
4	0.00729	1.99	0.0110	1.46	0.0150	1.50	0.0076	2.00

Table 8: Convergence rates in space; implicit Strang splitting scheme, Carreau viscosity.

# refin (Δh)	$Err(\mathbf{u})$	$EOC(\mathbf{u})$	$Err(\nabla\mathbf{u})$	$EOC(\nabla\mathbf{u})$	$Err(\eta)$	$EOC(\eta)$	$Err(p)$	$EOC(p)$
	L^q -norm				L^2 -norm			
1	0.24469		0.0218		0.3068		0.0695	
2	0.07891	1.63	0.0796	1.45	0.1186	1.37	0.0529	0.39
3	0.02867	1.46	0.0351	1.18	0.0514	1.21	0.0307	0.79
4	0.00709	2.02	0.0117	1.58	0.0190	1.43	0.0076	2.00

4.4.2 Experimental order of convergence in time

We will compute the EOC in time in the following way

$$EOC(\mathbf{u}) = \log_2 \frac{\left(\sum_{j=1}^N \|\mathbf{u}_{\Delta h, \Delta t}^j - \mathbf{u}_{\Delta h, \Delta t/2}^j\|_{L^q}^q / |\Omega_{\Delta h, \Delta t}^j|^q \right)^{1/q}}{\left(1/2 \sum_{j=1}^{2N} \|\mathbf{u}_{\Delta h, \Delta t/2}^j - \mathbf{u}_{\Delta h, \Delta t/4}^j\|_{L^q}^q / |\Omega_{\Delta h, \Delta t/2}^j|^q \right)^{1/q}} \quad \text{with} \quad T = \sum_{j=1}^N \Delta t = \Delta t N. \quad (83)$$

Moreover, we compute also the normalized relative $L^q(0, T; L^q(\Omega))$ error in time. This is defined by

$$Err(\mathbf{u}) = \frac{1}{T} \left(\sum_{j=1}^N \Delta t \left(\frac{\|\mathbf{u}_{\Delta h, \Delta t}^j - \mathbf{u}_{\Delta h, \Delta t/2}^j\|_{L^q}}{|\Omega_{\Delta h, \Delta t}^j|} \right)^q \right)^{1/q} \quad (84)$$

where $\mathbf{u}_{\Delta h, \Delta t}^j$ and $\Omega_{\Delta h, \Delta t}^j$ denotes the velocity and the computational domain associated with the time instant $j \Delta t$, respectively. Note that (83) and (84) are computed for a grid size Δh .

The EOC in time (83) was computed on a computational mesh consisting of 585 elements. Going from one time refinement to the finer one, the time step was halved. The time period for the computation was $t \in [0.2; 0.8]$ s and the initial time step was $\Delta t = 0.0125$ s. The initial computational domain is a rectangle, see Fig. 3.

Similarly as before, we compare explicit and implicit kinematic splitting scheme (Tabs.9, 10) and explicit and implicit Strang splitting scheme (Tabs.11, 12). We see that for the explicit kinematic splitting scheme the EOC is around first order. Considering the second order explicit Strang splitting technique, the convergence orders are improved. Working with the implicit kinematic splitting scheme, we obtained better convergence than in the explicit kinematic splitting scheme. Finally, in Tab.12, we see that the global errors are significantly smaller for the implicit Strang splitting scheme in comparison to the implicit kinematic splitting. Therefore we can note that the Strang splitting strategy gives better convergence results for both, the explicit and the implicit schemes.

Table 9: Convergence rates in time; explicit kinematic splitting, Carreau viscosity.

# refin (Δt)	$Err(\mathbf{u})$	$EOC(\mathbf{u})$	$Err(\nabla\mathbf{u})$	$EOC(\nabla\mathbf{u})$	$Err(\eta)$	$EOC(\eta)$	$Err(p)$	$EOC(p)$
	$L^q(L^q)$ -norm				$L^2(L^2)$ -norm			
2/1	0.0132		0.0088		0.0060		0.1422	
3/2	0.0070	0.92	0.0046	0.93	0.0041	0.55	0.0697	1.03
4/3	0.0042	0.74	0.0030	0.61	0.0016	1.36	0.0336	1.05

Table 10: Convergence rates in time; implicit kinematic splitting, Carreau viscosity.

# refin (Δt)	$Err(\mathbf{u})$	$EOC(\mathbf{u})$	$Err(\nabla\mathbf{u})$	$EOC(\nabla\mathbf{u})$	$Err(\eta)$	$EOC(\eta)$	$Err(p)$	$EOC(p)$
	$L^q(L^q)$ -norm				$L^2(L^2)$ -norm			
2/1	0.1532		0.1600		0.2706		0.4332	
3/2	0.0705	1.12	0.0747	1.10	0.2000	0.44	0.2286	0.92
4/3	0.0218	1.69	0.0234	1.67	0.0915	1.13	0.0683	1.74

Table 11: Convergence rates in time; explicit Strang splitting, Carreau viscosity.

# refin (Δt)	$Err(\mathbf{u})$	$EOC(\mathbf{u})$	$Err(\nabla\mathbf{u})$	$EOC(\nabla\mathbf{u})$	$Err(\eta)$	$EOC(\eta)$	$Err(p)$	$EOC(p)$
	$L^q(L^q)$ -norm				$L^2(L^2)$ -norm			
2/1	0.0195		0.0081		0.0234		0.1539	
3/2	0.0077	1.34	0.0024	1.75	0.0089	1.40	0.0712	1.11
4/3	0.0044	0.83	0.0013	0.90	0.0054	0.72	0.0315	1.18

Table 12: Convergence rates in time; implicit Strang splitting, Carreau viscosity.

# refin (Δt)	$Err(\mathbf{u})$	$EOC(\mathbf{u})$	$Err(\nabla\mathbf{u})$	$EOC(\nabla\mathbf{u})$	$Err(\eta)$	$EOC(\eta)$	$Err(p)$	$EOC(p)$
	$L^q(L^q)$ -norm				$L^2(L^2)$ -norm			
2/1	0.0578		0.0609		0.1140		0.2411	
3/2	0.0241	1.26	0.0243	1.32	0.0441	1.37	0.0896	1.43
4/3	0.0088	1.44	0.0078	1.64	0.0173	1.35	0.0297	1.60

4.5 HEMODYNAMIC WALL PARAMETERS

In this subsection we will compare several important hemodynamic wall parameters for different constitutive models as well as different reference geometries. Hemodynamic indices that help to predict areas sensitive to the stenotic plaque danger are the wall shear stress function (WSS) and the oscillatory shear index (OSI). The WSS is a local hemodynamic factor that is closely related to the occurrence of atherosclerosis. It is defined by

$$\text{WSS} := \tau_w = -(\mathbf{T}\mathbf{n}) \cdot \mathbf{n}^\perp, \quad (85)$$

where \mathbf{n} is the unit outward normal vector and \mathbf{n}^\perp denotes the unit tangential vector. The OSI measures pointwisely the temporal oscillations of WSS and is computed with the formula

$$\text{OSI} := \frac{1}{2} \left(1 - \frac{\int_0^T \tau_w \, dt}{\int_0^T |\tau_w| \, dt} \right). \quad (86)$$

It is known that the range of WSS in a normal artery is from [1.0, 7.0] Pa and in the venous system it is from [0.1, 0.6] Pa, see [35]. The regions of artery that are athero-prone, i.e. stimulates an atherogenic phenotype, are in the range of ± 0.4 Pa. On the other hand, WSS greater than 1.5 Pa induces an anti-proliferative and anti-thrombotic phenotype and therefore is found to be athero-protective. However, in the range of [7, 10] Pa high-shear thrombosis is likely to be found.

In the experiments shown in Figs. 13- 17, the physiological flow rates (Fig. 7) as well as physiological values for viscosity parameters (Tab. 2) were prescribed. In Fig. 13 we see the distribution of WSS for different time instants during the cardiac cycle along the moving boundary of stenosed vessel. The peak values of WSS (with exception of the time instant $t = 0.36$ s) correspond to the narrowed area of stenosed vessel. We see that the magnitude of the WSS differs with respect to time in the cardiac pulse cycle. In the systolic acceleration phase maximum ($t = 0.15$ s) the lower WSS area is at the beginning of vessel and behind the stenosis. In this period no reversed flow occurs and the WSS belongs to the athero-protective range. Different situation happens in the systolic minimum, i.e. at the end of systolic deceleration phase ($t = 0.36$ s). Negative values of WSS along the moving boundary are visible. In both cases we observe that the WSS corresponding to the non-Newtonian model gives higher extremal values. Passing the diastolic maximum a more complex behaviour can be seen. At $t = 0.58$ s two reversed flows develop. In the remaining phase, see $t = 0.90$ s, the magnitude of WSS is low, but not negative. Again, the non-Newtonian viscosities seem to elevate the values of WSS approaching the athero-protective range.

In Fig. 14 the WSS evolution for bifurcation reference geometry (Fig. 6) is presented. At each time instant a period of negative flow around the sinus bulb is visible. In the area of bifurcation divider and carotid sinus we observe that the non-Newtonian rheology elevates the extremal values of WSS. Moreover,

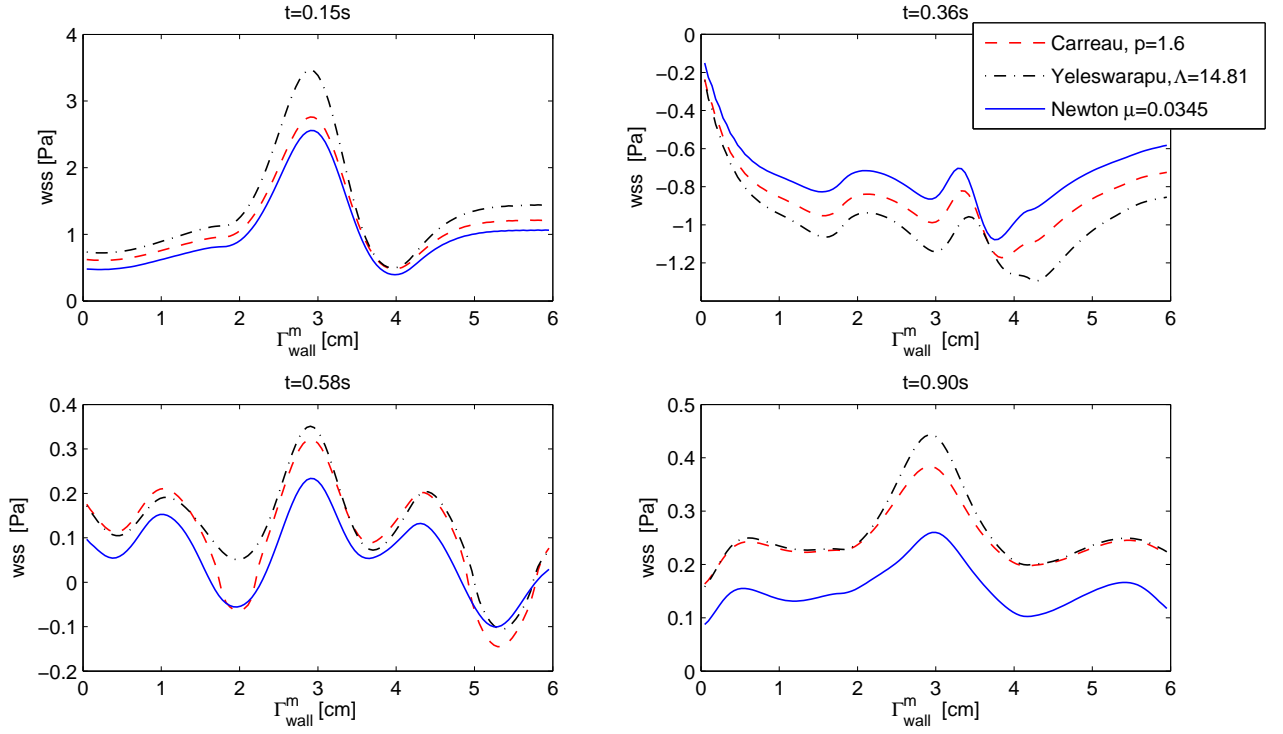


Figure 13: WSS along Γ_{wall} for stenotic vessel geometry at several time instants.

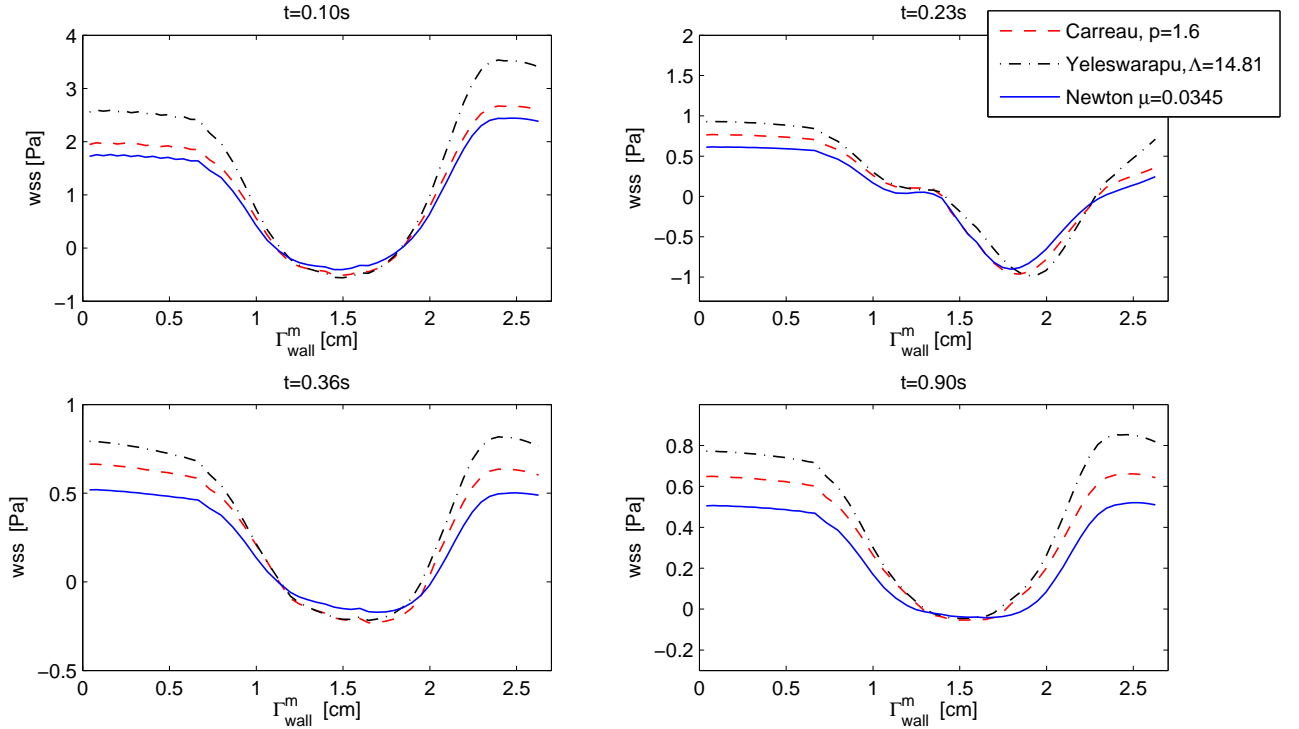


Figure 14: WSS along Γ_{wall}^m for bifurcation geometry at several time instants.

the magnitude of WSS falls into the atherosclerotic range around the sinus bulb area. This confirms the observations from clinical praxis, see [35].

The WSS distribution at several points on the moving boundary for bifurcation geometry and

stenosed geometry is demonstrated in Figs. 15, 16, respectively. Points of measurement correspond to: $x \approx 0.6$ cm for the common carotid artery, $x \approx 1.2$ cm for the proximal to the internal carotid artery, $x \approx 1.6$ cm for the mid-carotid sinus bulb, $x \approx 2.0$ cm for the end of carotid sinus bulb and $x \approx 2.5$ cm for the internal carotid artery. In the case of stenosed vessel, the WSS was measured in front of the stenosis $x \approx 1.8$ cm, in the maximal stenosed point $x \approx 3.0$ cm and after the stenosis $x \approx 4.0$ cm.

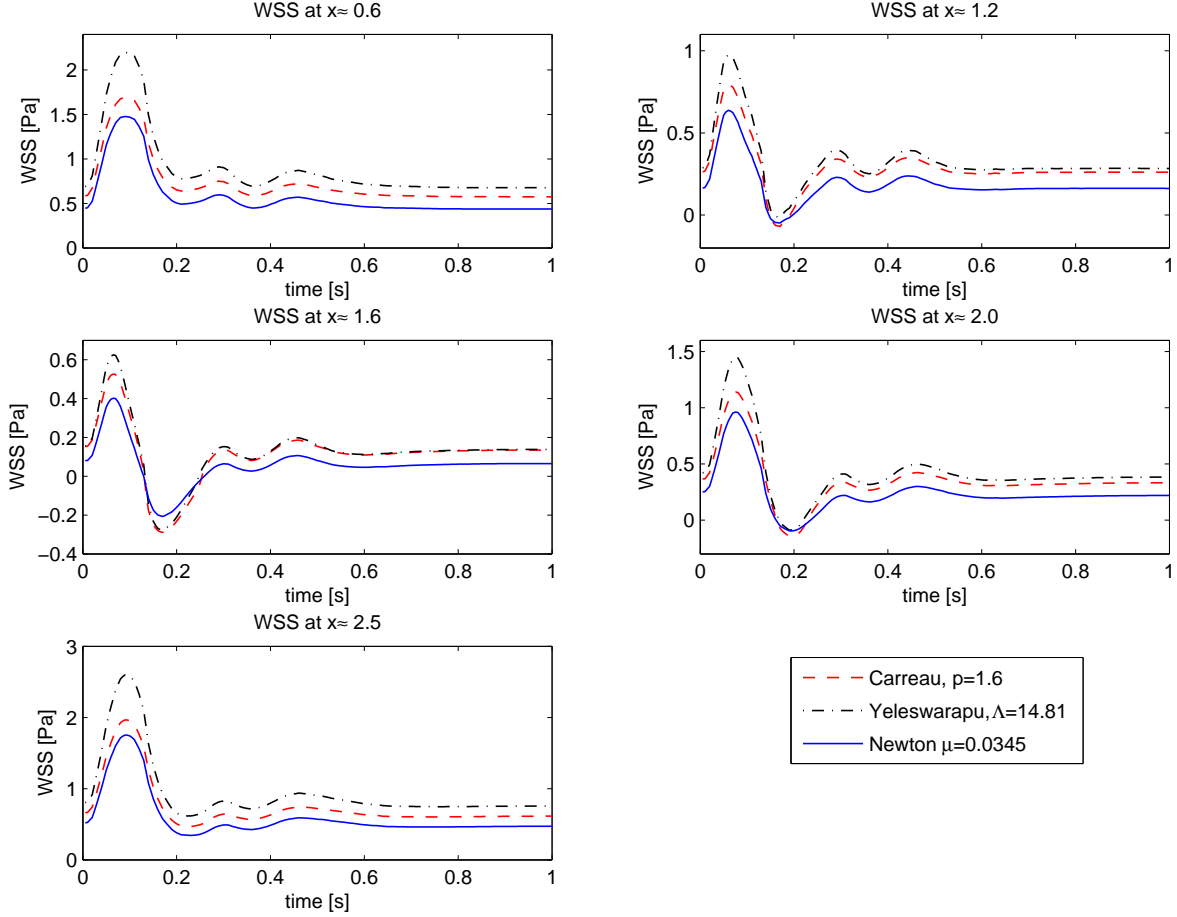


Figure 15: WSS at five different positions along Γ_{wall}^m for the period of one heart beat; bifurcation geometry.

The evolution curves of the WSS, see Fig. 15, at the common carotid artery ($x \approx 0.6$ cm) and the external carotid artery ($x \approx 2.5$ cm) have similar shape as the prescribed flow rate, see Fig. 7 left. They belong to the athero-protective range (i.e. WSS is typically larger than 0.4 Pa in these parts of artery). Approaching the bifurcation divider (at points $x \approx 1.2$ cm, $x \approx 1.6$ cm and $x \approx 2.0$ cm) we observe a reversed flow period with negative values of WSS, which is mostly athero-prone. Moreover, analyzing the curves in Fig. 15, we observe that the non-Newtonian rheology seems to be more athero-protective than the Newtonian one. The non-Newtonian rheology yields larger extremal values of WSS and shortens the periods of reversed flow.

Analysing the plots of the WSS evolution in sampling points for stenotic geometry, see Fig. 16, we can obtain the following information: the narrowed part of vessel corresponding to the point $x = 3$ cm yields higher values of WSS than at $x = 1.8$ cm and $x = 4.2$ cm (before and after the stenosis). Moreover, due to the large negative flow period in the iliac flow rate the values of WSS belong mostly to the athero-prone range (with exception of the systolic peak phase and the systolic minimum phase). Similarly to the bifurcation geometry (Fig. 15), higher extrema in the peaks of the flow are followed by higher WSS for the non-Newtonian models.

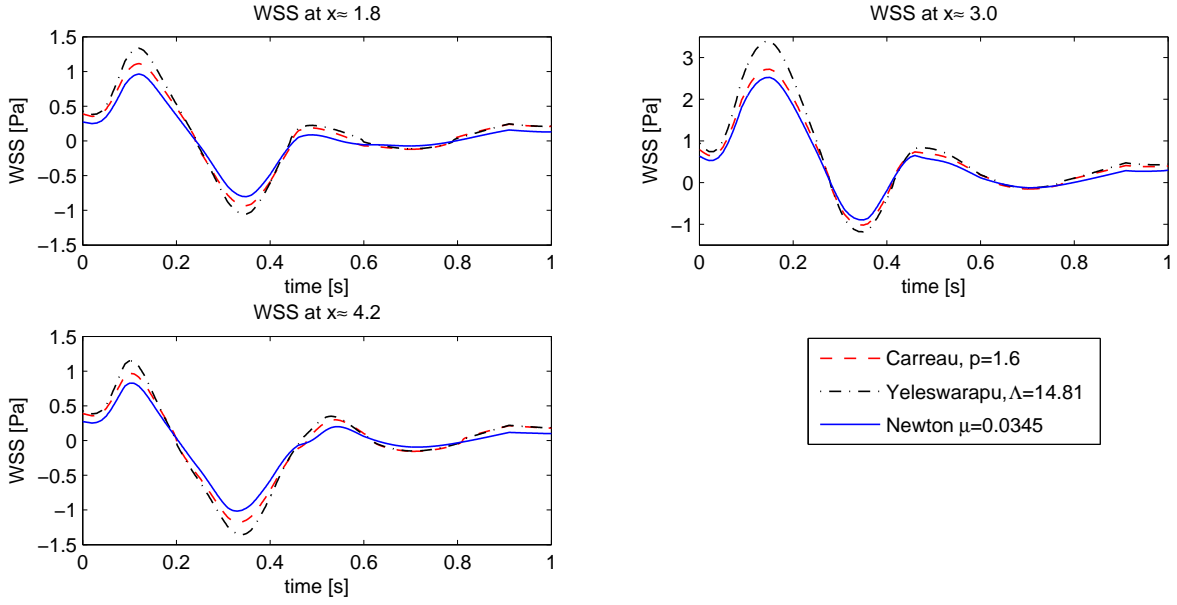


Figure 16: WSS at three different positions along Γ_{wall}^m for the period of one heart beat; stenotic geometry.

The results shown in Figs.13-16 confirm dependence of the shear stress distribution on a given geometry. Consecutively, the WSS is one of the important parameters for the prediction of stenotic danger.

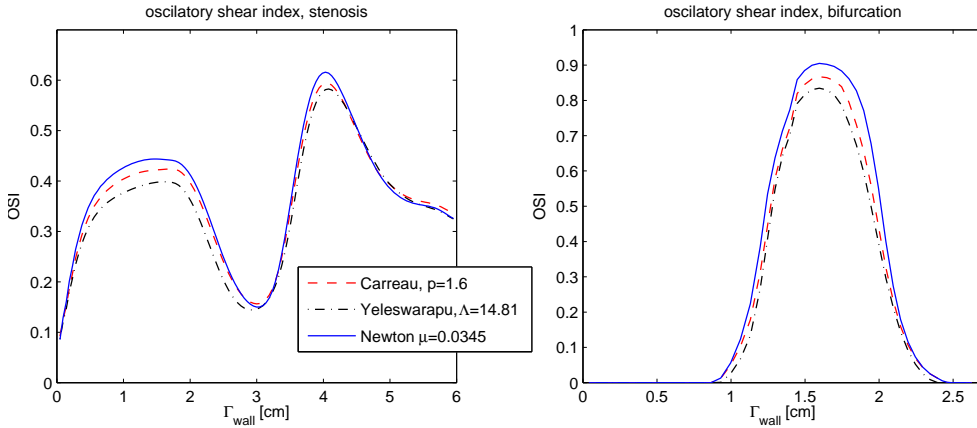


Figure 17: OSI along Γ_{wall} . Left: stenosed geometry, right: bifurcation geometry.

Finally, in Fig.17 the dependence of the OSI index on position and rheology is presented. Since the OSI measures the change of WSS with respect to the direction, high values of this index indicate regions with pulsatile WSS. Fig.17 (left) confirms our assumption that in the case of the iliac stenosed artery the reversed flow occurs along the whole boundary. Due to the high-shear flow in the stenosed region, direction-varying WSS appears in particular behind the stenosed area. This is clearly visible in the measurements of the OSI. In Fig.17 (right) it can be observed that the reversed flow appears preferentially in the carotid sinus. Indeed, the OSI index increases and the peak corresponds to the mid-carotid sinus point. Moreover, in both, the stenotic and the bifurcation reference geometry, the Newtonian rheology causes more oscillations of the WSS (for comparison see the areas of reversed flow in Fig.14, points $x = 1.2$ cm, $x = 1.6$ cm, $x = 2.0$ cm).

4.6 APPLICATION TO THREE-DIMENSIONAL FLOW

In this subsection we illustrate a potential applicability of the kinematic splitting algorithm for three-dimensional fluid-structure interaction problems. To this end we consider three-dimensional viscous in-

compressible fluid governed by the Navier-Stokes equations (1) interacting with a thin flexible viscoelastic structure located on one part of the fluid boundary, see also [19] for theoretical results on existence of a global weak solution of analogous fluid-structure interaction model.

Let us consider a three-dimensional computational domain $\Omega_t \subset \mathbb{R}^3$;

$$\Omega_t := \{(x_1, x_2, x_3) \in \mathbb{R}^3, t \in I : 0 < x_1 < L_1, 0 < x_2 < L_2, 0 < x_3 < R_0(x_1, x_2) + \eta(x_1, x_2, t)\}$$

occupied by a Newtonian fluid. We set $\omega := (0, L_1) \times (0, L_2)$. Let Γ_{wall}^0 be the fluid-structure interface at $t = 0$; i.e.,

$$\Gamma_{wall}^0 := \{(x_1, x_2, x_3) \in \mathbb{R}^3 : (x_1, x_2) \in \omega, x_3 = R_0(x_1, x_2)\}.$$

We model the deformable part of the boundary by the classical linear elasticity theory for transverse motions of a membrane, modified by including viscous effects, cf. also analogous model in [19]. We take structure to be clamped, but more general boundary conditions can be used as well. The equation describing time evolution of transversal displacement η ; $\eta(x_1, x_2, t) \in \mathbb{R}$

$$\frac{\partial^2 \eta}{\partial t^2} - a\Delta\eta - c\Delta\frac{\partial \eta}{\partial t} = H(\mathbf{u}, p) \quad \text{on } \Gamma_{wall}^0 \quad (87)$$

is accompanied by the following boundary and initial conditions

$$\begin{aligned} \eta &= 0 \quad \text{on } \partial\omega, t \in I \\ \eta &= 0, \quad \frac{\partial \eta}{\partial t} = \mathbf{u}_0|_{\Gamma_{wall}^0} \cdot \mathbf{e}_3 \quad \text{on } \Gamma_{wall}^0, t = 0, \end{aligned} \quad (88)$$

where \mathbf{e}_3 is a unit vector in the x_3 -, i.e. transversal, direction.

Analogously as for two-dimensional problem, cf. (8), $H(\mathbf{u}, p)$ represents the forces exhibited by the normal fluid stress on the elastic structure and transformed to Γ_{wall}^0 . The kinematic coupling condition follows from the fact that the viscous fluid adheres to the structure

$$\mathbf{u} = \left(0, 0, \frac{\partial \eta}{\partial t}\right)^T \quad \text{on } \Gamma_{wall}(t), \quad (89)$$

where

$$\Gamma_{wall}(t) := \{(x_1, x_2, x_3) \in \mathbb{R}^3 : (x_1, x_2) \in \omega, x_3 = R_0(x_1, x_2) + \eta(x_1, x_2, t)\}$$

The application of the kinematic splitting algorithm yields the following hydrodynamic and elastic operators, respectively.

$$\mathbf{Operator A} \text{ (hydrodynamic)} \begin{cases} \text{fluid solver } (\mathbf{u}, p), \\ \xi := u_3|_{\Gamma_{wall}}, \\ \frac{\partial \xi}{\partial t} = c\Delta\xi + H(\mathbf{u}, p) \end{cases} \quad (90)$$

$$\mathbf{Operator B} \text{ (elastic)} \begin{cases} \frac{\partial \eta}{\partial t} = \xi, \\ \frac{\partial \xi}{\partial t} = a\Delta\eta + G(R_0), \end{cases} \quad (91)$$

where $G(R_0) := a\Delta R_0$.

In Figure 18 we present results of numerical simulations obtained for the above three-dimensional FSI problem. We have implemented the kinematic splitting (90), (91) within the COMSOL Multiphysics 4.2 software package, where three-dimensional Navier-Stokes solver and three-dimensional mesh movement are available. We have applied COMSOL's Laminar Flow Solver for fluid, $\Delta\mathbf{u}$ Mathematics Solver for the structure equation and Deformed Geometry Solver (DG) for mesh movement. Further, we impose the Dirichlet boundary conditions for fluid at the inflow part. Inflow velocity has the maximum value 16 cm/s and is multiplied by $\sin(\pi t)$ function to model time dependent inflow, $t \in I$. On the outflow part

the normal stress is set to 0. We use the no-slip boundary condition for the remaining parts of boundary $\partial\Omega_t - (\Gamma_{in} \cup \Gamma_{out} \cup \Gamma_{wall})$.

Time discretization of the operator A is realized by the BDF 2 method, for space discretization the finite element method with $P1$ -bubble+ $P1$ elements is applied. Structure equation is approximated by $P2$ finite elements. Multifrontal massive parallel sparse direct solver (MUMS) is applied to solve the resulting linear algebraic systems. The experiments presented below are computed by means of the implicit kinematic splitting method (70).

For the computational domain the following parameters have been used: $L_1 = 8\text{cm}$, $L_2 = 1\text{cm}$, $R_0(x_1, x_2) = 1\text{cm}$. Further, we set the fluid viscosity to 0.0345 P and density to $1\text{ g}\cdot\text{cm}^{-3}$. For structure we use the following parameters: wall thickness is $h = 0.1\text{cm}$, wall density is $\rho_w = 1.1\text{g}\cdot\text{cm}^{-3}$, Timoshenko's factor is $\kappa = 1$, Poisson's ratio $\tilde{\xi} = 0.5$, $E = 0.75 \times 10^6\text{ Pa}$, viscoelasticity coefficient $\gamma = 0.2 \times 10^6$. Using analogous formulae as for two-dimensional case, cf. (9), we get the corresponding coefficients in the structure equation (87).

Computational domain for fluid is discretized by 60 915 tetrahedral elements. In Figure 18 we present results of fluid-structure interaction simulations at different time instants $t = 0.2, 0.4, 0.6, 0.8, 1.0, 1.2, 1.4$ and $t = 1.6\text{s}$. We depict velocity magnitudes, velocity vectors as well as streamlines.

5 CONCLUSION

In this paper we have presented theoretical and experimental analysis of the kinematic splitting algorithm for the fluid-structure interaction with application in hemodynamics. The mathematical model includes simplified but physiologically motivated geometries such as stenosed vessel and stenotic vessel bifurcation and captures the non-Newtonian behaviour of blood.

It is well-known that some partitioned fluid-structure interaction algorithms may have problems due to the added mass effects, cf. [14, 18, 24, 30, 40, 53]. Our approach, based on the kinematic boundary conditions, belongs to the class of loosely-coupled partitioned techniques, cf. also [27]. Using the energy estimates we have analysed stability of the kinematic coupled fluid-structure interaction scheme and shown that it is stable without any additional subiterations. Consequently, its computational efficiency is improved. In the stability analysis the crucial role of the geometric conservation law condition has been pointed out. We were able to show that using the implicit backward Euler discretization in time for the fluid equation and the second order Newmark scheme for the structure the kinematic splitting scheme is conditionally stable. Indeed, a stability condition gives some restriction on time step. Moreover, if the midpoint rule is used for the approximation of the convective term with the grid velocity in the fluid equations the unconditional stability of kinematic splitting has been proven.

Theoretical results were confirmed by a series of numerical experiments. The experimental order of convergence tests indicate the higher order of accuracy and even show smaller global errors than those obtained by the global iterative method. Experimental analysis of hemodynamic wall parameters confirms dependence of the WSS and the OSI on the vessel geometry. Moreover, we have observed that the non-Newtonian rheology plays a significant role for the hemodynamic indices. Although the qualitative character for both the Newtonian and the non-Newtonian fluids was similar, the results were quantitatively different.

Acknowledgements

This research has been financed by the European Union's 6th Framework Programme Reference under the Contract no. DEASE: MEST-CT-2005-021122, the Center for Computational Sciences in Mainz, the German Science Foundation under the project ZA 613/1-1 and by the German Academic Exchange Service DAAD. The authors gratefully acknowledge this support.

APPENDIX

A. REMARKS ON COMPUTATION OF THE BOUNDARY TERMS

In what follows all derivations are formal, i.e. we assume enough smooth functions, such that the corresponding integrals exist. The boundary term arising from the convective part has the form

$$-\frac{1}{2} \int_{\partial\Omega_t} |\mathbf{u}|^2 (\mathbf{u} - \mathbf{w}) \cdot \mathbf{n} \, dS = \int_{\Gamma_{in}} \left(\frac{1}{2} |\mathbf{u}|^2 \right) u_1 \, dx_2 - \int_{\Gamma_{out}} \left(\frac{1}{2} |\mathbf{u}|^2 \right) u_1 \, dx_2. \quad (92)$$

Here the velocity \mathbf{w} is defined in such a way that $\mathbf{w}|_{\Gamma_{wall}} = \mathbf{u}|_{\Gamma_{wall}}$, $\mathbf{w}|_{\Gamma_{sym}} = 0$ and $(\mathbf{u} \cdot \mathbf{n})|_{\Gamma_{sym}} = 0$. The stress tensor boundary term reads as follows

$$\begin{aligned} \frac{1}{\rho_f} \int_{\partial\Omega_t} (\mathbf{T} \mathbf{u}) \cdot \mathbf{n} \, dS &= \frac{1}{\rho_f} \int_{\Gamma_{wall}} (\mathbf{T} \mathbf{u}) \cdot \mathbf{n} \, dl + \frac{1}{\rho_f} \int_{\Gamma_{sym}} (\mathbf{T} \mathbf{u}) \cdot \mathbf{n} \, dS \\ &+ \int_{\Gamma_{in}} \left(-\frac{P_{in}}{\rho_f} + \frac{1}{2} |\mathbf{u}|^2 \right) (-u_1) dx_2 + \int_{\Gamma_{out}} \left(-\frac{P_{out}}{\rho_f} + \frac{1}{2} |\mathbf{u}|^2 \right) u_1 dx_2. \end{aligned} \quad (93)$$

Considering $\mathbf{n} = (0, -1)^T$, $\frac{\partial u_1}{\partial x_2} = 0$ and $u_2 = 0$ on Γ_{sym} we get $\int_{\Gamma_{sym}} (\mathbf{T} \mathbf{u}) \cdot \mathbf{n} \, dS = 0$. In order to rewrite the integral over Γ_{wall} we can proceed in the following way: we transform the external forces from Γ_{wall} to Γ_{wall}^0 and for each surface element $d\sigma_0 \in [0, 2\pi) \times \Gamma_{wall}^0$ we use the structure equation

$$\frac{\partial^2 \eta}{\partial t^2} - a \frac{\partial^2 \eta}{\partial x_1^2} + b\eta - c \frac{\partial^3 \eta}{\partial t \partial x_1^2} = -\frac{(\mathbf{T} + P_{ext} \mathbf{I}) \mathbf{n} \cdot \mathbf{e}_r}{\rho_s h} \frac{R}{R_0} \frac{\sqrt{1 + (\partial_{x_1} R)^2}}{\sqrt{1 + (\partial_{x_1} R_0)^2}} + a \frac{\partial^2 R_0}{\partial x_1^2} \quad (94)$$

with parameters a, b, c defined in (9). Consecutively, we have

$$\begin{aligned} \int_{\Gamma_{wall}} (\mathbf{T} \mathbf{u}) \cdot \mathbf{n} \, dl &= \frac{1}{2\pi} \int_0^{2\pi} \int_{\Gamma_{wall}} \frac{(\mathbf{T} \mathbf{n}) \cdot \mathbf{e}_r u_2}{R} \, d\sigma \\ &= \frac{1}{2\pi} \int_0^{2\pi} \int_{\Gamma_{wall}^0} \frac{(\mathbf{T} \mathbf{n}) \cdot \mathbf{e}_r u_2}{R_0} \frac{R}{R_0} \frac{\sqrt{1 + (\partial_{x_1} R)^2}}{\sqrt{1 + (\partial_{x_1} R_0)^2}} \, d\sigma_0 \\ &= -\frac{\rho_s h}{2\pi} \int_0^{2\pi} \int_{\Gamma_{wall}^0} \frac{1}{R_0} \left(\frac{\partial^2 \eta}{\partial t^2} - a \frac{\partial^2 \eta}{\partial x_1^2} + b\eta - c \frac{\partial^3 \eta}{\partial t \partial x_1^2} \right) \frac{\partial \eta}{\partial t} \, d\sigma_0 \\ &\quad - \frac{1}{2\pi} \int_0^{2\pi} \int_{\Gamma_{wall}^0} \frac{(P_{ext} \mathbf{I} \mathbf{n}) \cdot \mathbf{e}_r u_2}{R_0} \frac{R}{R_0} \frac{\sqrt{1 + (\partial_{x_1} R)^2}}{\sqrt{1 + (\partial_{x_1} R_0)^2}} \, d\sigma_0 \\ &\quad + \frac{a \rho_s h}{2\pi} \int_0^{2\pi} \int_{\Gamma_{wall}^0} \frac{1}{R_0} \frac{\partial^2 R_0}{\partial x_1^2} u_2 \, d\sigma_0. \end{aligned} \quad (95)$$

Here $d\sigma \in [0, 2\pi) \times \Gamma_{wall}$ and $d\sigma = R d\theta dl$. In (95) we have used the following equality: $(\mathbf{T} \mathbf{u}) \cdot \mathbf{n} = (\mathbf{T} \mathbf{n}) \cdot \mathbf{e}_r u_2$ on Γ_{wall} . The term containing external pressure can be transformed back to the Γ_{wall} as follows

$$\begin{aligned} -\frac{1}{2\pi} \int_0^{2\pi} \int_{\Gamma_{wall}^0} \frac{(P_{ext} \mathbf{I} \mathbf{n}) \cdot \mathbf{e}_r u_2}{R_0} \frac{R}{R_0} \frac{\sqrt{1 + (\partial_{x_1} R)^2}}{\sqrt{1 + (\partial_{x_1} R_0)^2}} \, d\sigma_0 &= -\frac{1}{2\pi} \int_0^{2\pi} \int_{\Gamma_{wall}} \frac{(P_{ext} \mathbf{I} \mathbf{n}) \cdot \mathbf{e}_r u_2}{R} \, d\sigma \\ &= - \int_{\Gamma_{wall}} \frac{P_{ext} u_2}{\sqrt{1 + (\partial_{x_1} R)^2}} \, dl \approx - \int_{\Gamma_{wall}} \frac{P_{ext} u_2}{\sqrt{1 + (\partial_{x_1} R_0)^2}} \, dl, \end{aligned} \quad (96)$$

where we have assumed that $\mathbf{n} \cdot \mathbf{e}_r \approx [1 + (\partial_{x_1} R_0)^2]^{-1/2}$. Altogether, summing up the contributions in (92) and (93) we obtain the boundary terms presented in (22) with $\mathbf{v} = \mathbf{u}$.

B. DISCRETE GRONWALL'S LEMMA [54]

Let $\Delta t, g_0, a_n, b_n, c_n, \gamma_n$ be sequences of non-negative numbers for $n \geq 0$. If the following inequality holds

$$a_n + \Delta t \sum_{i=0}^n b_i \leq \Delta t \sum_{i=0}^n \gamma_i a_i + \Delta t \sum_{i=0}^n c_i + g_0,$$

then for all $n \geq 0$ we have

$$a_n + \Delta t \sum_{i=0}^n b_i \leq \left[\Delta t \sum_{i=0}^n c_i + g_0 \right] \exp \left\{ \Delta t \sum_{i=0}^n \sigma_i \gamma_i \right\},$$

where $\Delta t \leq \frac{1}{\gamma_i}$ and $\sigma_i := \frac{1}{1 - \gamma_i \Delta t}$ for $i = 0, \dots, n$.

References

- [1] Anand M., Rajagopal K., Rajagopal K.R.: A model incorporating some of the mechanical and biochemical factors underlying clot formation and dissolution in flowing blood, *J. Theor. Med.* 5(3-4) (2003), 183–218.
- [2] Ardakani S.S.J., Jafarnejad M., Firoozabadi B., Saidi M.S.: Investigation of wall shear stress related factors in realistic carotid bifurcation geometries and different flow conditions, *Scientia Iranica, Transaction B: Mech. Eng.* 17 (2010), 358–366.
- [3] Badia S., Nobile F., Vergara C.: Fluid-structure partitioned procedures based on Robin transmission conditions, *J. Comput. Phys.* 227 (14) (2008), 7027–7051.
- [4] Badia S., Nobile F., Vergara C.: Robin-Robin preconditioned Krylov methods for fluid-structure interaction problems, *Comput. Meth. Appl. Mech. Eng.* 198 (2009), 2768–2784.
- [5] Behbahani M., Behr M., Hormes M., Steinseifer U., Arora D., Coronado O., Pasquali M.: A review of computational fluid dynamics analysis of blood pumps, *Eur. J. Appl. Math.* 20 (2009), 363–397.
- [6] Behbadani M., Behr M., Nicolai M., Probst M.: Towards shape optimization for ventricular assist devices using parallel stabilized FEM, *In: Proceedings of the NIC Symposium*, 325–331, Jülich, 2008.
- [7] Bodnár T., Sequeira A., Prosi M.: On the shear-thinning and viscoelastic effects of blood flow under various flow rates, *Appl. Math. Comput.* 217 (2011), 5055–5067.
- [8] Bodnár T., Sequeira A.: Numerical study of the significance of the non-Newtonian nature of blood in steady flow through a stenosed vessel, *In: Rannacher R. et al. (Eds.), Advances in Mathematical Fluid Mechanics*, 83–104, Springer Verlag, 2010.
- [9] Boulakia M., Cazeau S., Fernández Varela M.A., Gerbeau J.F., Zenzemi N.: Mathematical modeling of electrocardiograms: a numerical study, *Ann. Biomed. Eng.* 38(3) (2010), 1071–1097.
- [10] Bukač M., Čanić S., Glowinski, R., Tambača, J., Quaini, A.: Fluid-structure interaction in blood flow capturing non-zero longitudinal structure displacement, *J. Comput. Phys.* 235 (2013), 515–541.
- [11] Burman E., Fernández M.A.: Stabilization of explicit coupling fluid-structure interaction involving fluid incompressibility, *Comput. Meth. Appl. Mech. Eng.* 198 (2009), 766–794.

- [12] Calvez V., Huout J.G., Meunier N., Raoult A., Rusnáková G.: Mathematical and numerical modeling of early atherosclerotic lesions, *ESAIM: Proceedings*, 30 (2010), 1–14.
- [13] Čanić S., Tambača J., Guidoboni G., Mikelić A., Hartley C.J., Rosenstrauch D.: Modeling viscoelastic of arterial walls and their interaction with pulsatile blood flow, *SIAM J. Appl. Math.* 67(1) (2006), 164–193.
- [14] Causin P., Gerbeau J.F., Nobile F.: Added-mass effect in the design of partitioned algorithms for fluid-structure problems, *Comput. Meth. Appl. Mech. Eng.* 194 (2005), 4506–4527.
- [15] Chambolle A., Desjardin B., Esteban M.J., Grandmont C.: Existence of weak solutions for unsteady fluid-plate interaction problem, *J. Math. Fluid. Mech.* 4(3) (2005), 368–404.
- [16] Deparis S., Discacciati M., Fourestey G., Quarteroni A.: Fluid-structure algorithms based on Steklov-Poincaré operators, *Comput. Meth. Appl. Mech. Eng.* 195 (41-43) (2006), 5797–5812.
- [17] Diening L., Prohl A., Růžička M.: Semi-implicit Euler scheme for generalized Newtonian fluids, *SIAM J. Numer. Anal.* 44(3) (2006), 1172–1190.
- [18] Fernández M.A.: Coupling schemes for incompressible fluid-structure interaction: implicit, semi-implicit and explicit, *Bol. Soc. Esp. Mat. Apl.* 55 (2011), 59–108.
- [19] Fernández M.A., Gerbeau J.-F., Grandmont C.: A projection semi-implicit scheme for the coupling of an elastic structure with an incompressible fluid, *J. Numer. Meth. Eng.* 69 (2007), 794–821.
- [20] Filo J., Zaušková A.: 2D Navier-Stokes equations in a time dependent domain with Neumann type boundary conditions, *J. Math. Fluid. Mech.* 12 (2010), 1–46.
- [21] Formaggia L., Nobile F.: A stability analysis for the arbitrary Lagrangian Eulerian formulation with finite elements, *East. W. J. Numer. Math.* 7(2) (1999), 103–131.
- [22] Formaggia L., Moura A., Nobile F.: On the stability of the coupling of 3D and 1D fluid-structure interaction models for blood flow simulations, *M2AN, Mathem. Model. Num. Anal.* 41(4) (2007), 743–769.
- [23] Formaggia L., Quarteroni A., Veneziani A.: *Cardiovascular Mathematics*, Springer, Milano, 2009.
- [24] Forster C., Wall W., Ramm E.: Artificial added mass instabilities in sequential staggered coupling of nonlinear structures and incompressible viscous flow, *Comp. Meth. Appl. Mech. Eng.* 196(7) (2007), 1278–1293.
- [25] Galdi G.P., Rannacher R., Robertson A.M., Turek S.: *Hemodynamical Flows. Modelling, Analysis, Simulation*. Oberwolfach-Seminars, Vol. 37, Birkhäuser, 2008.
- [26] Glowinski R.: Numerical Methods for Fluids (Part 3), In: Ciarlet P.G. et al. (Eds.) *Handbook of Numerical Analysis*, Vol. VI, Elsevier, Amsterdam, 2003.
- [27] Guidoboni G., Glowinski R., Cavallini N., Čanić S.: Stable-loosely coupled-type algorithm for fluid-structure interaction on blood flow, *J. Comput. Phys.* 228 (18) (2009), 6916–6937.
- [28] Gresho P.M., Sani R.L.: On pressure boundary conditions for the incompressible Navier-Stokes equations, *Int. J. Numer. Meth. Fluid* 7 (1987), 1111–1145.
- [29] Hademenos G.J., Massoud T.F.: Biophysical mechanisms of stroke. *American Heart Association*, Vol. 28 (1997), 2067–2077.
- [30] Hundertmark-Zaušková A., Lukáčová-Medvidřová M.: Numerical study of shear-dependent non-Newtonian fluids in compliant vessels, *Comput. Math. Appl.* 60 (2010), 572–590.

- [31] Hundertmark-Zaušková A., Lukáčová-Medviďová M., Nečasová Š.: On the existence of fluid-structure interaction of non-Newtonian shear-dependent fluid in compliant vessels, *Preprint University of Mainz*, 2011.
- [32] Janela J., Moura A., Sequeira A.: A 3D non-Newtonian fluid-structure interaction model for blood flow in arteries, *J. Comput. Appl. Math.* 234 (2010), 2783–2791.
- [33] Leeson P.: *Cardiac Imaging*, Oxford University Press, 2011.
- [34] Lesoinne M., Farhat Ch.: Geometric conservation laws for flow problems with moving boundaries and deformable meshes, and their impact on aeroelastic computations, *Comput. Meth. Appl. Mech. Eng.* 134(1-2) (1996), 71–90.
- [35] Malek A.M., Alper A.L., Izumo S.: Hemodynamic shear stress and its role in atherosclerosis, *J. Am. Med. Assoc.* 282 (1999), 2035–2042.
- [36] Málek J., Nečas J., Rokyta M., Ružička: Weak and Measure-valued Solutions to Evolutionary PDEs, *Chapman and Hall*, London, 1996.
- [37] Matthies H.G., Steindorf J.: Partitioned but strongly coupled iteration schemes for nonlinear fluid-structure interaction, *Comput. Struct.* 80 (27-30) (2002), 1991–1999.
- [38] Muha B., Canic S.: Existence of a weak solution to a nonlinear fluid-structure interaction problem modeling the flow of an incompressible, viscous fluid in a cylinder with deformable walls, *Arch. Rational Mech. Anal.* 207(3) (2013), 919-968.
- [39] Nobile F.: *Numerical approximation of fluid-structure interaction problems with application to haemodynamics*, PhD Thesis, EPFL Lausanne, 2001.
- [40] Nobile F., Vergara C.: An effective fluid-structure interaction formulation for vascular dynamics by generalized Robin conditions, *SIAM J. Sci. Comput.* 30(2) (2008), 731–763.
- [41] Nägele S.: *Mehrgitterverfahren für die inkompressiblen Navier-Stokes Gleichungen im laminaren und turbulenten Regime unter Berücksichtigung verschiedener Stabilisierungsmethoden*, PhD Thesis, Rupprechts-Karl University Heidelberg, 2003.
- [42] Nägele S., Wittum G.: On the influence of different stabilisation for incompressible Navier-Stokes equations, *J. Comput. Phys.* 224 (2007), 100–116.
- [43] Perego M., Veneziani A., Vergara C.: Variational approach for estimating the compliance of the cardiovascular tissue: an inverse fluid-structure interaction problem, *SIAM J. Sci. Comput.* 33(3) (2011), 1181–1211.
- [44] Perktold K., Resch M., Reinfried O.P.: Three-dimensional numerical analysis of pulsatile flow and wall shear stress in the carotid artery bifurcation, *J. Biomech.* 24(6) (1991), 409-420.
- [45] Raback P., Ruokolainen J, Lyly M., Järvinen E.: Fluid-structure interaction boundary conditions by artificial compressibility, *ECCOMAS Computational Fluid Dynamics*, Swansea, 2001.
- [46] Rusnáková G.: *Numerical modelling of fluid-structure interaction with application in hemodynamics*, PhD Thesis, JGU Mainz, UPJŠ Košice, 2012.
- [47] Sequeira A., Santos R.T., Bodnár T.: Blood coagulation dynamics: mathematical modelling and stability results, *Math. Biosci. Eng.* 8(2) (2011), 425–443.
- [48] Soulis J.V., Giannoglou G.D., Chatzizisis Y.S., Seralidou K.V., Parcharidis G.E., Louridas G.E.: Non-Newtonian models for molecular viscosity and wall shear stress in a 3D reconstructed human left coronary artery, *Med. Eng. Phys.* 30(1) (2008), 9-19.

- [49] Steinman D.A., Loepping T.L., Tambasco M., Rankin R.N., Holdsworth D.W.: Flow pattern at the stenosed carotid bifurcation: effect of concentric versus eccentric stenosis, *Ann. Biomed. Eng.* 28 (2008), 415–423.
- [50] Tambača J., Kosor M., Čanić S., Paniagua D.M.D.: Mathematical modeling of vascular stents, *SIAM J. Sci. Comput.* 70(6) (2010), 1922–1952.
- [51] Taylor C.A., Hughes J.R., Zarins C.K.: Effect of exercise on hemodynamic conditions in the abdominal aorta, *J. Vasc. Surg.* 29(6) (1999), 1077–1089.
- [52] Vignon-Clementel I., Figueroa C.A., Jansen K.E., Taylor C.A.: Outflow boundary conditions for three-dimensional simulations of non-periodic blood flow and pressure fields in deformable arteries, *Comput. Meth. Appl. Mech. Eng.* 13(5) (2010), 625–640.
- [53] Quarteroni A., Formaggia L.: Mathematical Modelling and Numerical Simulation of the Cardiovascular System, In: Ciarlet P.G. et al. (Eds.), *Handbook of Numerical Analysis (Computational models for the human body)*, Vol. XII, Elsevier, 2004.
- [54] Quarteroni A., Valli A.: Numerical Approximation of Partial Differential Equations, *Springer Series in Computational Mathematics*, Springer, 2008.
- [55] Yeleswarapu K.K.: *Evaluation of continuum models for characterizing the constitutive behavior of blood*, PhD Thesis, University of Pittsburgh, 1996.
- [56] Yeleswarapu K.K., Kameneva M.V., Rajagopal K.R., Antaki J.F.: The flow of blood in tubes: theory and experiment, *Mech. Res. Comm.* 25(3) (1998), 257–262.

